Weather Clim. Dynam., 7, 2277–2303, 2026
https://doi.org/10.5194/wcd-7-2277-2026
© Author(s) 2026. This work is distributed under
the Creative Commons Attribution 4.0 License.

Weather and Climate Dynamics
Open Access
EGU

Vertical structure and dynamical regimes of extreme warm events in the Central Mediterranean: a three-dimensional analysis over Rome (Italy)

Annalisa Di Bernardino[1], **Stefano Casadio**[2], **Anna Maria Iannarelli**[2], **and Anna Maria Siani**[1]

[1]Physics Department, Sapienza University of Rome, Rome, 00185, Italy
[2]SERCO Italia SpA, Frascati, Rome, 00044, Italy

Correspondence: Annalisa Di Bernardino (annalisa.dibernardino@uniroma1.it)

Received: 9 July 2026 – Discussion started: 29 July 2026
Revised: 6 November 2026 – Accepted: 12 November 2026 – Published: 23 November 2026

Abstract. Climate change is rapidly accelerating the frequency of Extreme Warm Events (EWEs) across the Mediterranean, yet their vertical thermodynamic structure and dynamical evolution remain poorly understood. This study investigates the vertical patterns of EWEs over Rome during the 1991–2025 period using ERA5 temperature data at three strategic pressure levels representing distinct functional layers: 1000 hPa (near-surface), 500 hPa (middle troposphere), and 300 hPa (high troposphere).

EWEs were identified using daily mean air temperature exceeding the 90th percentile of the 1991–2020 climatological distribution, calculated with a 21 d moving window, at least at one of three selected pressure levels for four consecutive days. Event duration was defined as the number of consecutive days satisfying the persistence criterion, while mean thermal intensity was quantified as the event-averaged temperature anomaly relative to the reference climatology. Then, EWEs were classified using a K-means clustering approach. Their evolution was further investigated through precursor analysis, synoptic composites, and HYSPLIT backward trajectories. Five Extreme Warm Regimes (EWRs) were identified through the clustering, spanning from shallow boundary-layer warming to vertically coherent deep-column structures. These regimes naturally separate into two broader classes: vertically coupled events, characterized by warming throughout the tropospheric column, and vertically decoupled events, in which thermal anomalies remain confined to specific atmospheric layers. Spatial composite analysis and seasonal analysis confirm that these five configurations reflect physically robust, structurally stable, and recurring atmospheric modes across all seasons rather than artifacts of seasonal aggregation. Trend analysis reveals a marked increase in the frequency of vertically coupled regimes after 2015, while the average duration and mean thermal intensity of episodes have remained remarkably stable over the 35-year period. Representative case studies show that the coupled regimes develop through different pathways, involving persistent blocking, subsidence, and/or subtropical warm-air advection, while the remaining regimes maintain persistent vertical decoupling throughout their evolution.

Overall, these findings indicate a progressive climatic transition toward more vertically organized and synoptically controlled EWEs, providing key information on the physical nature of Mediterranean heat extremes that cannot be inferred from near-surface temperatures alone.

1 Introduction

The Mediterranean basin is widely recognized as a climate change hotspot (Giorgi, 2006), with surface air temperature having already reached approximately 1.5 °C above pre-industrial levels, outpacing the global average by roughly 0.4 °C (Cramer et al., 2018; Seneviratne et al., 2021). Sea surface temperatures (SST) follow a similar trend, with the Mediterranean Sea warming substantially faster than the global ocean. Mean Mediterranean SST increased by about 0.35 °C per decade during 1982–2019, corresponding to more than twice the global mean SST warming rate (Pastor et al., 2020; Seneviratne et al., 2021). Under high-emission sce-

narios (SSP5-8.5), climate projections consistently identify annual warming for the Mediterranean projected to exceed the global mean by about 20 %, while summer warming may reach 40 %–50 % above global rates, especially across the northern Mediterranean basin (Cos et al., 2022; Hassoun et al., 2025). In addition, the European State of the Climate (ESOTC) 2025 report indicated that the European continent has become increasingly susceptible to more frequent and more intense Extreme Warm Events (EWEs) due to alterations in large-scale atmospheric circulation (C3S/ECMWF and WMO, 2026). Furthermore, multi-model projections suggest a progressive intensification in the frequency, intensity, and duration of heatwaves (HWs) throughout the 21st century (Zittis et al., 2021; Cos et al., 2022).

The primary drivers of the development of EWEs include coupled large-scale atmospheric and oceanic circulation patterns, land-atmosphere feedback, and interannual thermal variability (Seneviratne et al., 2010; Stéfanon et al., 2014; C3S/ECMWF and WMO, 2026). In this context, the marked warming in the Arctic region (Arctic Amplification) has been proposed as a mechanism that could potentially alter mid-latitude atmospheric circulation by weakening the equator-to-pole temperature gradient (Francis et al., 2017; Coumou et al., 2018; C3S/ECMWF and WMO, 2026). However, its exact influence on the frequency, intensity, and persistence of European blocking events remains a subject of debate in the scientific community, as observational trends and climate model simulations often yield divergent results (Cohen et al., 2020; Previdi et al., 2021). As documented, European HWs are intrinsically linked to persistent high-pressure systems, which obstruct or divert mid-to-high latitude westerly winds for extended periods, thereby facilitating the intensification of thermal extremes (Woollings et al., 2018; Sousa et al., 2018). Beyond atmospheric dynamics, SST anomalies in the Atlantic Ocean and Mediterranean basin play a critical role in modulating the duration and intensity of HWs, suggesting a significant teleconnection between oceanic SST variations and extreme continental heat (Duchez et al., 2016; Capozzi et al., 2025).

Traditionally, research has focused on HWs occurring during the boreal summer, as this coincides with the annual peaks in air and sea surface temperatures. However, it is now evident that global warming is triggering an increase in warm anomalies across all seasons, with profound implications for ecosystems, biodiversity, and phenology (Perkins-Kirkpatrick and Lewis, 2020; Rousi et al., 2022; Mahecha et al., 2024). Furthermore, most studies have approached HWs primarily as surface-level phenomena, largely to assess their impacts on human health and socio-economic sectors (Margolis, 2020; Lin and Li, 2026). While valuable, this approach overlooks the complex atmospheric processes governing the intensity and persistence of Mediterranean heat extremes, highlighting the need for a three-dimensional perspective (Lhotka and Kyselý, 2024). Recently, a growing body of literature has emphasized that heat extremes are inherently three-dimensional atmospheric features driven by complex vertical structures and circulation patterns (e.g., Miralles et al., 2014; Sousa et al., 2018; Hotz et al., 2026). Hotz et al. (2026) also provided a comprehensive global baseline of vertical temperature anomaly profiles during HWs, showing that extreme thermal anomalies exhibit substantial vertical variability and are often decoupled between the Planetary Boundary Layer (PBL) and the free troposphere. While upper-tropospheric thermal extremes do not directly impact terrestrial ecosystems or human health at the surface, their diagnostic value lies in their role as dynamical indicators of large-scale atmospheric patterns (Pfahl et al., 2015; Zschenderlein et al., 2019). In fact, analysing high-level events that do not reach the surface allows us to isolate the near-surface and lower-tropospheric mechanisms (such as cold-air advection, marine boundary layer stratification, or sea-breeze regime) that decouple the near-surface atmospheric layer from intense mid-tropospheric ridging. In addition, high-tropospheric anomalies frequently act as dynamic precursors to synoptic-scale blockings, offering a diagnostic window into the vertical evolution and downward propagation of thermodynamic anomalies prior to full-column coupling (Sousa et al., 2018). Analysing the entire vertical column allows for a comprehensive classification of warm events, distinguishing deep, surface-impacting HWs from dynamically isolated upper-tropospheric thermal features (Lhotka and Kyselý, 2024; Hassoun et al., 2025).

In this study, it is worth noticing that a clear distinction is provided among three related but conceptually distinct phenomena:

- *Heatwave* (HW): persistent period of high near-surface air temperature exceeding a high, specific percentile threshold for a minimum multi-day period, consistent with standard surface climatological definitions (World Meteorological Organization and World Health Organization, 2015);

- *Extreme Warm Event* (EWE): episodes during which daily mean air temperature exceeds the level-specific 90th percentile threshold at a given isobaric level (from the surface up to 300 hPa). This term encompasses both classical surface-based HWs and vertically limited warm anomalies that are not necessarily experienced also at the surface;

- *Extreme Warm Regime* (EWR): vertical profile configuration derived from the co-occurrence of EWEs at multiple pressure levels. While an EWE identifies events at a given pressure level, an EWR characterizes the coherent vertical structure of the warming (distinguishing deep-column coupled extremes from surface-confined or upper-tropospheric isolated layers), which reflects the broader three-dimensional synoptic-scale patterns evaluated through composite and trajectory analyses.

Building upon this framework, the present study defines the degree of thermodynamic coupling among atmospheric layers during an EWE, ranging from anomalies confined to specific atmospheric layers to fully coupled tropospheric structures. A critical yet under-explored aspect is the lead-lag relationship between these layers: distinguishing between "top-down" intensification, driven by synoptic-scale subsidence, and "bottom-up" thermodynamics, where surface processes may precede or amplify tropospheric warming, a structural dynamic also recently highlighted by Hotz et al. (2026). The approach proposed here intentionally includes vertically confined warm regimes to investigate the full spectrum of atmospheric thermal structures associated with Mediterranean warm extremes and their dynamical coupling.

This study addresses this knowledge gap by leveraging ERA5 pressure-level reanalysis data for the city of Rome (Italy), covering the period 1991–2025. Rome represents a compelling case study where large-scale atmospheric forcing interacts with Mediterranean coastal processes and urban microclimate. The main objectives of this paper are to: (i) identify the vertical regimes of Mediterranean EWEs using a multi-level clustering framework; (ii) investigate their long-term temporal evolution, seasonal expansion, and changes in vertical coupling over the last 35 years; and (iii) interpret the physical mechanisms governing each regime by combining precursor analysis, synoptic diagnostics, and backward air-mass trajectories.

The paper is structured as follows: Sect. 2 outlines the datasets and the multi-level diagnostic framework; Sect. 3 presents and discusses the long-term trends, the EWR classification, and the physical mechanisms driving the selected case studies. Finally, Sect. 4 summarizes the main conclusions of the study.

2 Materials and methods

This Section describes the datasets, diagnostic framework, and analytical procedures adopted to investigate the vertical structure and evolution of EWEs over Rome. A schematic overview of the complete methodological workflow is presented in Fig. 1, illustrating the sequence of steps from data processing and event detection to clustering, synoptic characterization, and precursor analysis.

2.1 Study area description

Rome (41.90° N, 12.49° E) is located in the central-western part of the Italian Peninsula, approximately 27 km inland from the coast of the Tyrrhenian Sea (Fig. 1). The city's geographical setting is characterized by a complex topography, settled along the Tiber River valley and flanked by the Apennine Mountains to the east and the volcanic Alban Hills to the southeast. This positioning makes Rome a strategic location for investigating the interplay between synoptic-scale and mesoscale coastal dynamics.

According to the Köppen-Geiger classification, Rome experiences a typical Mediterranean climate class (Csa, temperate climate), with hot, dry summers and mild, wet winters (Beck et al., 2018). In addition, the urban structure of Rome contributes to the development of a pronounced Urban Heat Island (UHI) (Di Bernardino et al., 2025). From a dynamic perspective, the city is frequently influenced by the northward extension of the North African High, which brings warm, dry air masses aloft that progressively gain moisture in the lower troposphere as they cross the marine path across the Mediterranean (Gobbi et al., 2019). The vertical structure of the atmosphere over Rome is further modulated by the interaction between the urban footprint and the Tyrrhenian sea-breeze circulation. During summer, near-surface HWs, high solar irradiance, and strong land-sea thermal contrasts drive a robust daytime sea-breeze front that penetrates inland, establishing a stable thermal stratification that can temporarily decouple the near-surface layer from the free troposphere (Di Bernardino et al., 2021, 2023). However, under intense synoptic subsidence and weak background ventilation, this daytime coastal buffering is often overwhelmed, while nocturnal cooling is strongly suppressed by the summer UHI (Cecilia et al., 2023; Di Bernardino et al., 2023). In transition and winter seasons, although land-sea thermal gradients are weaker and coastal breezes are less vigorous, local urban microclimates and mesoscale flows remain active, though lower-tropospheric thermal anomalies are governed more directly by synoptic-scale advection. By focusing on this site, the study captures the co-existence and mutual feedback among large-scale subsidence, synoptic warm-air advection, and urban-coastal microclimates, providing a comprehensive view of the EWE development in a vulnerable Mediterranean metropolitan area.

2.2 ERA5 Reanalysis dataset

Atmospheric data used in this study were obtained from the ERA5 reanalysis, the fifth-generation global atmospheric reanalysis produced by the European Centre for Medium-Range Weather Forecasts (ECMWF). ERA5 integrates a wide range of observations with numerical weather prediction models through data assimilation, providing a temporally and spatially consistent reconstruction of the Earth's atmospheric state from the surface to the upper atmosphere (Hersbach et al., 2020).

To investigate the thermodynamic structure of the troposphere over Rome, hourly ERA5 fields covering 1 January 1991–31 December 2025 were retrieved. The vertical domain was characterized using 15 pressure levels, from 1000 to 300 hPa, with a constant vertical decrement of 50 hPa. These levels were dynamically subsetted according to the specific analytical requirements of the study: (i) three core pressure levels (1000, 500, and 300 hPa) were used for the identifica-

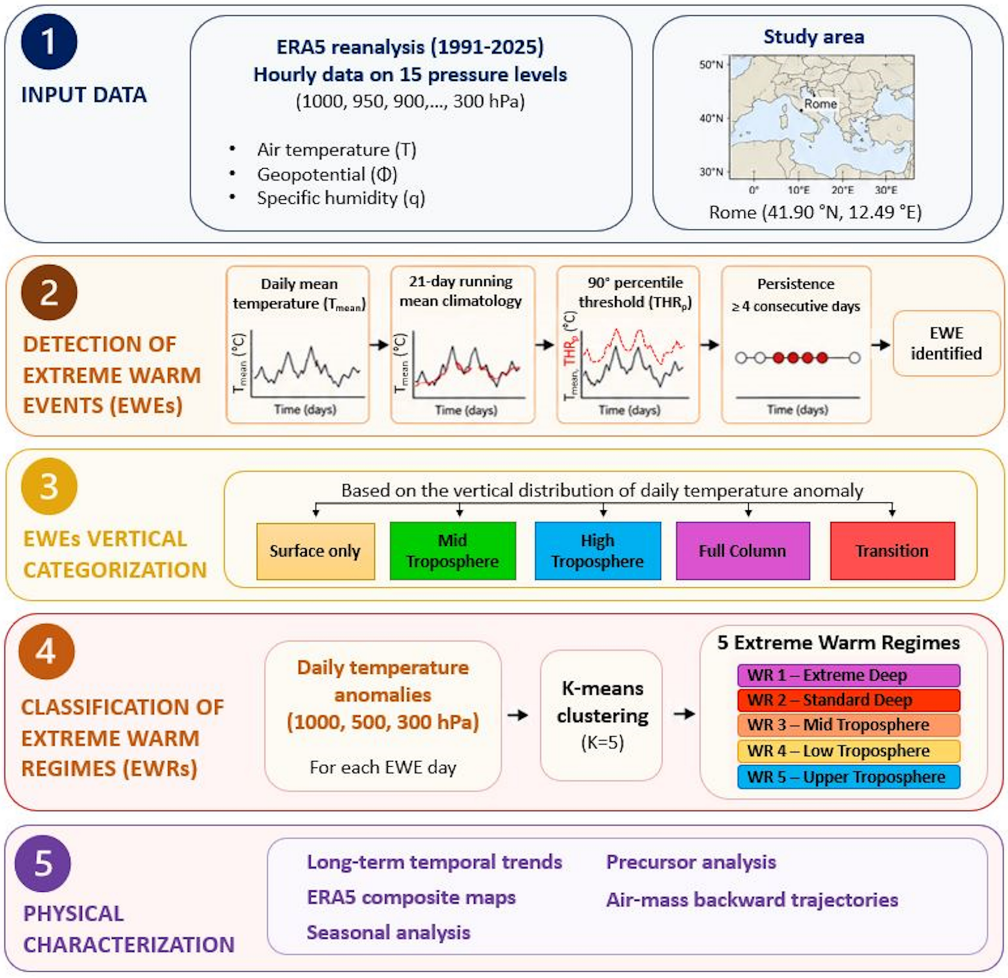

Figure 1. Schematic overview of the methodological framework adopted to investigate EWEs over Rome during the 1991–2025 period. ERA5 reanalysis data were used to identify EWEs using both percentile-based and persistence-based detection criteria. Events were first grouped according to their vertical thermal structure and subsequently classified into EWRs using K-means clustering.

tion and vertical classification of EWEs; (ii) four key reference levels (1000, 850, 500, and 300 hPa) were selected to analyse long-term climatological and temporal trends; and (iii) the complete 15-level vertical profile was exploited to resolve high-resolution time-height cross-sections during the precursory phases and individual case studies.

This selection is based on physical and statistical considerations. In fact, adjacent pressure levels in high-resolution reanalyses exhibit strong vertical collinearity. Including all 15 levels in the clustering algorithm's distance matrix may introduce redundant variance, which tends to degrade cluster separation and excessively flatten regime boundaries. In addition, the three selected levels strategically sample three distinct functional layers of the atmosphere. Specifically, the 1000 hPa level captures near-surface thermodynamic conditions and PBL processes directly influenced by surface heat sources/sinks. Because the target domain over the metropolitan area of Rome lies in low-elevation coastal terrain (surface elevation < 100 m a.s.l.), the 1000 hPa level consistently resides above the physical surface, avoiding artificial sub-surface reanalysis extrapolations common over elevated topography. The 850 hPa level serves as a standard diagnostic for air-mass characterization. Being located above the PBL, it is largely decoupled from local surface influences, including UHI effects. It can therefore be used to assess whether lower-tropospheric thermal extremes are driven by regional warm-air advection (associated with the poleward transport of subtropical air masses within the 850–700 hPa layer) or by local processes such as large-scale adiabatic compression. The 500 hPa level represents the mid-troposphere and provides information on whether heat extremes are accompanied by large-scale subsidence, ridge amplification, or warm-core anticyclonic structures. Finally, the 300 hPa level characterizes upper-tropospheric circulation and allows the identification of jet-stream variability, Rossby-wave activity, and high troposphere dynamical perturbations that may contribute to

persistent atmospheric blocking and warm episodes over the Mediterranean basin (Sousa et al., 2018; Rousi et al., 2022).

The following variables were selected at each level: air temperature (T, °C) to quantify the intensity and vertical extension of thermal anomalies, geopotential (Φ, $m^2\,s^{-2}$) used to derive the geopotential height ($Z = \Phi/g_0$ where $g_0 = 9.81\,m\,s^{-2}$ is the Earth's mean gravitational acceleration) to detect weather synoptic systems, and specific humidity (q, $kg\,kg^{-1}$) to assess the moisture-related thermodynamic properties of the air masses.

Data extraction was centred on the metropolitan area of Rome. Given the native ERA5 horizontal resolution ($\sim 0.25° \times 0.25°$; ~ 31 km), the extracted fields should be interpreted as spatially representative atmospheric conditions over the broader urban-coastal environment. This approach is particularly suitable for investigating large-scale and vertically integrated atmospheric structures, while local urban-scale processes remain only partially resolved within the reanalysis framework (Zhu et al., 2021; Nogueira et al., 2022; Hersbach and NCAR staff, 2025).

2.3 Evaluation of long-term temporal trends

The long-term evolution of the vertical atmospheric structure over Rome was evaluated by applying the Mann-Kendall (MK) test (Mann, 1945; Kendall and Gibbons, 1962) to the timeseries of monthly anomalies of air temperature, geopotential height, and specific humidity at four representative pressure levels: 1000, 850, 500, and 300 hPa, chosen to characterize the entire tropospheric column.

As recommended by the World Meteorological Organization (WMO), monthly anomalies were calculated with respect to the reference climatological period 1991–2020 (World Meteorological Organization, 2017, 2022). For each specific calendar month, the anomaly was derived by subtracting the corresponding multi-year monthly mean from the individual monthly value. This procedure effectively eliminates the dominant annual cycle, allowing for a robust assessment of the underlying forced climatic signal (Yue and Wang, 2004; Sadhukhan et al., 2022). Therefore, the original MK test was applied (rather than its seasonal version) as the prior removal of the monthly mean ensures that the test detects whether a statistically significant, monotonic upward or downward trend exists in the residuals, without making assumptions about data normality. Complementarily, the magnitude of the temporal trend was quantified using Sen's Slope estimator (Hirsch and Slack, 1984), providing the rate of change per decade. By computing the median of all pairwise slopes, Sen's slope yields a robust linear rate of change that is highly resilient to single-year extreme outliers. All statistical assessments were carried out with a significance level $\alpha = 0.05$ (the null hypothesis of no-trend is rejected if the p-value is less than 5 %).

2.4 Identification and classification of Extreme Warm Events (EWEs)

To characterize the vertical structure of EWEs, a multi-level identification framework was developed. The climatological reference period follows the 1991–2020 WMO standard normal, which is used to derive the pressure-level-specific temperature thresholds described below. The detection algorithm is applied to daily mean temperature (T_{mean}) at three pressure levels (p): 1000, 500, and 300 hPa, selected to represent the near-surface, middle, and high troposphere, as discussed above. Unlike conventional HW detection methods, the proposed framework also identifies persistent warm anomalies confined to the middle or high troposphere. In doing so, upper-level EWEs are treated not as "failed" surface HWs but as distinct thermodynamic regimes governed by upper-tropospheric wave dynamics and adiabatic compression, providing a clear benchmark for when and why synoptic forcing successfully penetrates the PBL. This allows the simultaneous identification of both vertically coupled and decoupled warm events, thereby capturing the full vertical structure of atmospheric thermal extremes.

For each day of the year (d) and pressure level (p), a dynamical threshold (THR_p) was defined using the 90th percentile ($T_{p,90,\mathrm{ref}}$) of the daily mean temperature distribution during the 1991–2020 reference period, using a 21 d moving window ($d \pm 10$ d) centred on each calendar day:

$$\mathrm{THR}_p(d) = T_{p,90,\mathrm{ref}}\,(d \pm 10), \tag{1}$$

This moving-window approach is applied to calculate the daily climatological mean and the corresponding 90th-percentile temperature threshold, allowing it to capture the seasonal variability of air temperature. The 90th percentile baseline follows standard climatological definitions established by the Expert Team on Climate Change Detection and Indices (ETCCDI; Zhang et al., 2011), endorsed by WMO, and widely applied in IPCC assessment frameworks (Seneviratne et al., 2021). While adopting a stricter percentile threshold (e.g., 95th or 99th) would isolate rarer and more extreme events, the 90th percentile threshold was deliberately selected to balance detection sensitivity with statistical robustness. In a multi-level diagnostic framework, this sample size is essential for ensuring robust cluster convergence, stable precursor composites, and reliable trend evaluations, particularly for vertically confined or transient regimes aloft. Consequently, thermal extremes are evaluated relative to the evolving climatological background, allowing robust identification of anomalously warm conditions throughout the year (Di Bernardino et al., 2023, 2024).

An EWE is identified when the following two conditions are simultaneously satisfied:

1. Intensity: T_{mean} exceeds THR_p at least at one of the three reference pressure levels p (1000, 500, and 300 hPa);

2. Persistence: the intensity criterion is satisfied, at the same pressure level, for at least four consecutive days.

The 4 d persistence criterion was adopted to ensure that only sustained warm anomalies are retained, in line with the persistence requirements commonly used in HW identification, while excluding short-lived warm episodes. While many HW indices employ a 3 d threshold, adopting here a four d persistence requirement serves specific synoptic and methodological purposes. Synoptically, short-lived transient ridges and fast-propagating Rossby waves over the Central Mediterranean typically persist for 2 to 3 d, meaning that a 4 d threshold ensures that identified events reflect quasi-stationary, high-amplitude synoptic structures rather than transient thermal fluctuations. Methodologically, requiring sustained 4 d persistence allows sufficient time for multi-day thermodynamic feedbacks to fully manifest throughout the vertical column, while simultaneously improving signal-to-noise separation in the subsequent clustering analysis. Consequently, events interrupted by one or more days below the corresponding threshold are treated as separate EWEs rather than a single continuous event. Event persistence was first assessed independently at each pressure level. Warm episodes occurring simultaneously or with temporal overlap across different layers were then combined into a single EWE, enabling the characterization of its evolving structure throughout the tropospheric column.

Finally, to disentangle the relative contributions of synoptic-scale atmospheric processes and near-surface feedback, each day within an identified EWE was assigned to one of five mutually exclusive classes, according to the hierarchical classification presented in Table 1. The functional characterizations assigned to each class reflect the vertical anomaly structure of the event rather than prescriptive physical outcomes. Events confined to lower levels represent shallow warm anomalies governed primarily by surface energy fluxes, PBL dynamics, or shallow advection under weak synoptic forcing, rather than conventional HWs. Conversely, mid- and high-tropospheric EWEs serve as upper-level thermodynamic indicators of passing ridges or wave dynamics aloft that remain decoupled from the PBL.

To quantitatively assess each EWE, the daily mean temperature deviation from the 21 d running climatological mean for each day (t) belonging to a single event for each pressure level p for $p \in \{1000, 500, 300\,\text{hPa}\}$ is defined as:

$$\Delta T_{\text{mean},p}(t) = T_{\text{mean},p}(t) - T_{\text{mean},p,\text{ref}}(t), \quad (2)$$

In addition, the event-averaged temperature deviation relative to each pressure level p is denoted as $\overline{\Delta T_p}$. To complement this intensity metric and better discriminate among different event structures, the intra-event temporal variability of the anomaly at each pressure level is quantified by computing its standard deviation σ_{T_p}.

Table 1. Vertical classification of EWE categories.

EWE Category	Temperature condition
Surface Only	$T_{\text{mean},1000} > \text{THR}_{1000} \wedge$ $T_{\text{mean},500} \leq \text{THR}_{500} \wedge$ $T_{\text{mean},300} \leq \text{THR}_{300}$
Mid Troposphere	$T_{\text{mean},1000} \leq \text{THR}_{1000} \wedge$ $T_{\text{mean},500} > \text{THR}_{500} \wedge$ $T_{\text{mean},300} \leq \text{THR}_{300}$
High Troposphere	$T_{\text{mean},1000} \leq \text{THR}_{1000} \wedge$ $T_{\text{mean},500} \leq \text{THR}_{500} \wedge$ $T_{\text{mean},300} > \text{THR}_{300}$
Full Column	$T_{\text{mean},1000} > \text{THR}_{1000} \wedge$ $T_{\text{mean},500} > \text{THR}_{500} \wedge$ $T_{\text{mean},300} > \text{THR}_{300}$
Transition	Other combinations of $T_{\text{mean},p} > \text{THR}_p$

2.5 Identification and classification of Extreme Warm Regimes (EWRs)

To objectively identify and characterize the distinct vertical atmospheric configurations associated with EWEs, a K-means clustering analysis was applied to the population of identified EWE days using daily temperature anomalies at the three reference pressure levels (1000, 500, and 300 hPa). The identified clusters correspond to recurrent vertical profiles of temperature anomalies, representing both vertically coupled and vertically decoupled warm regimes.

To determine the optimal number of EWRs (i.e., the number of clusters K) objectively and avoid subjective selection bias, two complementary validation metrics were evaluated: the Elbow Method and Silhouette Analysis (see Fig. A1). The Elbow Method assesses the within-cluster sum of squares (inertia) as a function of K. The optimal number of clusters corresponds to the point where the rate of decrease sharply changes (the "elbow"), indicating that adding further clusters yields diminishing returns in explaining total variance. The Silhouette Analysis measures cluster cohesion and separation by comparing the mean distance of an observation to other points within its own cluster against the mean distance to points in the nearest neighbouring cluster. As illustrated in Fig. A1b, $K = 5$ corresponds to a local maximum in the Silhouette score, coinciding with a clear inflection in the inertia curve (Fig. A1a). Sensitivity tests using $K = 4$ and $K = 6$ were also evaluated. Selecting $K = 4$ the *Standard Deep* and *Low Troposphere* regimes were merged, masking the distinct surface-bound, bottom-up thermodynamics characteristic of lower-tropospheric events. Conversely, $K = 6$ splits vertically coupled clusters without revealing new physical processes, resulting in a lower overall silhouette score.

Table 2. List of the metrics adopted for the characterization of EWRs.

Metric	Definition
EWRs frequency (n days)	total number of EWE days
EWRs duration (n days)	average persistence of EWEs
Average temperature anomaly ($\overline{\Delta T}$, °C)	event-averaged temperature deviation relative to each pressure level p with respect to the reference climatological period
Cumulative Heat Index (CHI, °C d)	time-integral of temperature anomalies, evaluated over the entire duration of each EWE, used as a proxy of the thermodynamic load within the atmospheric column

Therefore, $K = 5$ provides an optimal balance between statistical separation and physical interpretability.

Moreover, to evaluate potential seasonal dependencies in the vertical structure and physical mechanisms of EWEs, a seasonal analysis was performed. Identified EWE days were partitioned into the four standard meteorological seasons: winter (DJF), spring (MAM), summer (JJA), and autumn (SON). The dual-metric validation framework (Elbow Method and Silhouette Analysis) was applied independently to each seasonal subset. The optimal cluster count yielded $K = 5$ for spring, autumn, and winter, whereas summer exhibited an optimal metric configuration at $K = 4$. To ensure methodological consistency across all temporal domains, facilitate direct comparison between seasonal regimes and the all-year baseline, and avoid masking distinct lower-tropospheric processes, $K = 5$ was retained for all seasonal clustering analyses.

Then, to further investigate potential climate-driven shifts in the distribution of the identified EWRs, the 35-year study period was subdivided into 5-year intervals, and the specific metrics presented in Table 2 were derived for each cluster (i.e., for each EWR) and temporal window.

Once the EWRs were clusterized, synoptic composite maps were generated using the ERA5 dataset to disentangle the synoptic atmospheric configurations and physical drivers associated with each EWR, using the geopotential height at 500 hPa (Z_{500}) and air temperature anomaly at 850 hPa (ΔT_{850}). Specifically, the Z_{500} field reflects the large-scale atmospheric circulation and provides information on whether the identified EWRs are associated with mid-tropospheric ridges, atmospheric blocking, troughs, or their synoptic-scale circulation features. Specifically, mid-tropospheric ridges are defined as open, high-amplitude poleward extensions of the Z_{500} geopotential height contours accompanied by a coherent thermal ridge, maintaining a continuous eastward phase speed without closed isolines or meridional flow reversals over the Central Mediterranean. Atmospheric blockings are characterized by persistent, quasi-stationary vortex (closed Z_{500} contours) that induce a local reversal of the meridional geopotential height gradient, forming classic Omega patterns that obstruct the westerly flow. This distinction ensures that composite circulation features are categorized accurately according to their kinematic and dynamical properties. ΔT_{850} is utilized as a standard diagnostic for identifying air-mass characteristics unaffected by immediate surface diurnal cycles, serving to detect the origin and intensity of lower-tropospheric warm-air advection. The use of the thermal anomaly rather than absolute temperature allows for a clear discrimination of the synoptic forcing from the strong seasonal cycle characteristic of the Mediterranean climate. Lower-tropospheric ΔT_{850} must be interpreted as the net thermodynamic response to both horizontal thermal advection and vertical air mass alteration (e.g., adiabatic subsidence heating beneath high-pressure systems). An elevated ΔT_{850} alone does not uniquely isolate horizontal warm-air advection from North Africa, as warm anomalies at 850 hPa can equally result from large-scale adiabatic compression (subsidence heating) beneath synoptic anticyclones, or from strong surface-driven convective entrainment. In regimes where ΔT_{850} coincide with high Z_{500} but weak horizontal advection, adiabatic subsidence under the ridge axis and local solar radiative heating act as the primary drivers of column warming.

2.6 Temporal evolution of precursor thermal anomaly

To characterize the evolution of multi-level vertical features in the tropospheric column preceding the onset of EWEs, a precursor analysis was developed. This approach tracks the progressive intensification, vertical alignment, and thermodynamic precursory pathways of the warming signal across different tropospheric layers during the days immediately leading up to the event initiation. For each EWE, the onset date (t_0) is defined as the first day of a persistent sequence (minimum 4 consecutive days) during which $T_{\mathrm{mean},p}(t) > \mathrm{THR}_p(t)$ at least at one of the target pressure levels p (1000, 500, and 300 hPa). The temporal window for the analysis of the preceding conditions spans a 4 d frame from t_{-3} to t_0, where t_{-n} represents the nth day prior to the official event onset (with $n = 1, 2, 3$).

To quantify the pre-onset thermodynamic behaviour, the cluster-averaged mean thermal anomaly ($\overline{\Delta T_p(t_{-n})}$) is computed by averaging at each level p the temperature anomalies across all N_C events belonging to a specific cluster:

$$\overline{\Delta T_p\,(t_{-n})} = \frac{1}{N_C}\sum_{i=1}^{N_C} \Delta T_{p,i}\,(t_{-n})\,, \tag{3}$$

where $\Delta T_{p,i}(t_{-n})$ represents the daily temperature anomaly recorded on day t_{-n} at pressure level p for the ith event belonging to a selected cluster.

2.7 Investigation of selected case studies

To bridge the gap between statistical clustering and atmospheric dynamics, a representative case study was selected for each EWR following the approach in Sect. 2.5. Rather than serving as a formal statistical validation of the clusters, these selected episodes act as observational exemplars designed to illustrate the detailed thermodynamic pathways and synoptic drivers characterizing each regime during extreme conditions. It is worth noticing that, since EWEs are transient phenomena, their vertical structure can dynamically evolve through different categories over time. To isolate the most representative and persistent fingerprint for each EWR, the chronologically continuous event exhibiting the maximum CHI value across the reference levels (1000, 500, and 300 hPa) was selected, prioritizing episodes where the dominant daily cluster ID matched the prevailing vertical category of the entire event. While individual events within the same EWR naturally exhibit variability in peak intensity, exact duration, and fine-scale trajectory pathways, selecting the maximum-CHI continuous episode ensures that the physical mechanisms governing the build-up and decay of the regime are captured at their peak expression.

The vertical evolution of each case study was investigated using the time-height cross-sections (Hovmöller diagrams) of temperature anomalies and equivalent potential temperature (θ_e). Temperature anomalies were calculated relative to the local mean of the 21 d window to isolate the warm core of the event. θ_e, assumed as a conservative tracer for both dry and pseudo-adiabatic processes, was calculated following the classical thermodynamic formulation as in Bolton (1980):

$$\theta_e = \theta \exp\left(\frac{L_v q}{c_p T}\right) \tag{4}$$

where θ is the potential temperature for dry air in K, L_v is the latent heat of evaporation (2406 kJ kg^{-1} at 313.15 K and 2501 kJ kg^{-1} at 273.15 K) and c_p is the specific heat of dry air at constant pressure (1005.7 J kg^{-1} K^{-1}).

The combined analysis of θ_e and temperature anomalies allows for the identification of air mass origins. Specifically, high θ_e values suggest the intrusion of moist tropical air masses, while relatively low θ_e values, concurrent with high thermal anomalies, indicate large-scale atmospheric subsidence, where the air mass warms via vertical compression while remaining significantly dry.

In addition, to disentangle the large-scale forcing, the synoptic-scale drivers of each event were characterized using ERA5 composite maps of Z_{500} and ΔT_{850}, averaged over the specific event duration.

Finally, to identify the geographical origin of the air masses and their vertical displacement, the Hybrid Single-particle Lagrangian Integrated Trajectory (HYSPLIT) model (Version 4.8), developed by the National Oceanic and Atmospheric Administration Air Resources Laboratory (NOAA ARL), was used to retrieve the backward trajectories of the air parcels arriving in Rome at 12:00 UTC of the day of maximum ΔT_{850} (Draxler and Rolph, 2010). Each backward trajectory was calculated for a 96 h duration, with arrival altitudes set at 500, 1500, and 5500 m above ground level to comprehensively sample the PBL, the lower troposphere, and the mid-tropospheric flow.

3 Results and discussion

3.1 Long-term temporal trends

The progressive warming observed over Rome is consistent with the accelerated climate change regional trends documented across the Mediterranean basin, as clearly reflected in the results from the MK test and Sen's slope estimates summarized in Table 3. According to the results of the MK test, all positive trends detected are statistically significant (p-value < 0.05). The analysis, conducted on monthly anomalies across the 1991–2025 period, and subsequently partitioned into meteorological seasons, highlights a robust, statistically significant upward trend in thermal anomalies (ΔT) throughout the entire tropospheric column on an annual basis, with warming rates ranging from +0.427 °C per decade at 300 hPa to +0.457 °C per decade close to the surface (1000 hPa).

This relatively uniform warming throughout the troposphere suggests that the observed climate signal is not confined to the PBL but affects the entire atmospheric column over the metropolitan area. However, the seasonal breakdown unveils a more complex picture. The summer season (JJA) exhibits the most intense warming across the vertical profile, with thermal anomaly trends peaking at +0.587 °C per decade at 300 hPa and remaining remarkably high down to the surface (+0.554 °C per decade). In addition, a significant warming signal is also observed in autumn (SON) and winter (DJF), with decadal trends paralleling summer values. These outcomes support the hypothesis of a seasonal stretching of summer-like synoptic configurations in autumn, effectively expanding the temporal window of regional vulnerability to EWEs.

This thermodynamic evolution is further supported by trends in geopotential-height anomalies (ΔZ). Marked positive trends are heavily concentrated in the mid-to-upper levels during both summer and autumn, peaking in the high troposphere (300 hPa) at +19.502 gpm per decade in autumn and +18.640 gpm per decade in summer. Notably, the absence of significant trends for ΔZ at 1000 hPa across all seasons suggests that the increasing frequency and severity of EWEs over the region are primarily governed by high troposphere dynamical intensification and enhanced synoptic-scale subsidence (ridge deepening), rather than shifts in mean surface pressure.

Specific humidity anomalies (Δq) show widespread and significant increases across almost all pressure levels and

Table 3. Decadal Sen's slope estimates obtained from the MK test applied to monthly atmospheric anomalies (1991–2025) relative to the 1991–2020 climatology. Sen's slopes are expressed as °C per decade for ΔT, gpm per decade for ΔZ, and g kg^{-1} per decade for Δq. Trends are denoted by symbols: ↑ (positive trend), ↓ (negative trend), and ↔ (no trend).

Variable	All year		Winter		Spring		Summer		Autumn	
	Slope	Trend	Slope	Trend	Slope	Trend	Slope	Trend	Slope	Trend
ΔT_{1000}	0.457	↑	0.494	↑	0.273	↑	0.554	↑	0.424	↑
ΔT_{850}	0.453	↑	0.496	↑	0.154	↔	0.582	↑	0.445	↑
ΔT_{500}	0.447	↑	0.393	↔	0.336	↑	0.496	↑	0.480	↑
ΔT_{300}	0.427	↑	0.290	↔	0.292	↑	0.587	↑	0.441	↑
ΔZ_{1000}	−0.138	↔	−3.075	↔	0.798	↔	−1.302	↔	1.750	↔
ΔZ_{850}	2.298	↑	−0.920	↔	2.386	↔	1.827	↔	3.988	↔
ΔZ_{500}	9.160	↑	5.415	↔	7.244	↔	10.250	↑	11.961	↑
ΔZ_{300}	15.795	↑	6.607	↔	12.313	↑	18.640	↑	19.502	↑
Δq_{1000}	0.265	↑	0.227	↑	0.174	↑	0.441	↑	0.273	↑
Δq_{850}	0.180	↑	0.134	↑	0.169	↑	0.295	↑	0.162	↑
Δq_{500}	0.033	↑	0.222	↑	0.034	↑	0.043	↑	0.046	↑
Δq_{300}	0.004	↑	0.002	↔	0.003	↑	0.004	↑	0.007	↑

seasons. The annual near-surface trend (+0.265 g kg^{-1} per decade) nearly doubles during summer (+0.441 g kg^{-1} per decade), consistent with the increased water-holding capacity of a warming atmosphere. This provides a higher latent heat content, which may critically alter atmospheric stability and amplify the overall intensity of EWEs (Di Bernardino et al., 2023).

3.2 Temporal frequency and multidecadal evolution of Extreme Warm Events (EWEs)

The application of the multi-level identification framework reveals substantial heterogeneity in the vertical structure of EWEs affecting the metropolitan area of Rome. According to the criteria summarized in Table 1, five mutually exclusive EWE categories were identified. A total of 1371 d were classified as EWE during the study period.

The thermodynamic nature of these classes is inferred from the vertical alignment of thermal anomalies. *Surface Only* EWEs point toward a vertical decoupling from the high troposphere synoptic circulation, where extremes might be amplified by local diabatic processes, such as UHI or soil moisture-temperature feedback. On the contrary, *Full Column* events are characterized by concurrent thermal anomalies across all atmospheric layers, from 1000 to 300 hPa. From a dynamic perspective, this configuration is consistent with deep-column warming, potentially associated with persistent subsidence and large-scale anticyclonic circulation. The *Mid Troposphere* and *High Troposphere* EWE categories serve as indicators of stratified forcing, such as warm-air advection driven by the northward extension of the North African High (typically peaking at 500 hPa) or transient dynamical pulses associated with jet-stream perturbations in the high troposphere. Finally, the *Transition* class successfully captures the complex structural evolution during the growth and decay phases of individual EWEs.

The temporal evolution of EWE typologies, presented in Fig. 2, shows a marked increase over the 1991–2025 period. While the early decades (1991–2010) are characterized by sporadic events dominated primarily by *Surface Only* or *High Troposphere* anomalies, the last decade (2015–2025) exhibits a marked change in the frequency and composition of EWE categories. Specifically, the total annual number of EWE days has escalated from 20–40 d per year in the 1990s to unprecedented peaks in recent years, exceeding 120 d in 2022, 130 d in 2023, and culminating in a historical maximum of over 160 d in 2024, i.e., more than four times the values observed during most of the 1990s. This rise reflects a widespread increase across all EWE categories. In particular, near-surface anomalies (*Surface Only*) show a marked and continuous rise throughout the period, while *Full Column* and *High Troposphere* events, which were comparatively rare in the first two decades, appear with noticeably higher frequency during the last decade. Overall, the increasing contribution of the *Full Column* category suggests a growing prevalence of vertically coupled warm anomalies over the study region, where synoptic-scale dynamical intensification dominates over localized boundary layer responses.

The temporal distribution of individual EWE days from 1991 to 2025 throughout the year (Fig. 3) illustrates both the intra-annual seasonality and a pronounced multi-decadal intensification of warm extremes throughout the tropospheric column. Seasonally, EWEs are distributed across the entire year, with high-tropospheric anomalies (*High Troposphere* category) frequently developing in spring and early summer as elevated thermodynamic precursors associated with upper-level ridge building. During the core summer months of July and August, these upper-level features increasingly transition into and co-occur with persistent *Full Column* and *Transition*

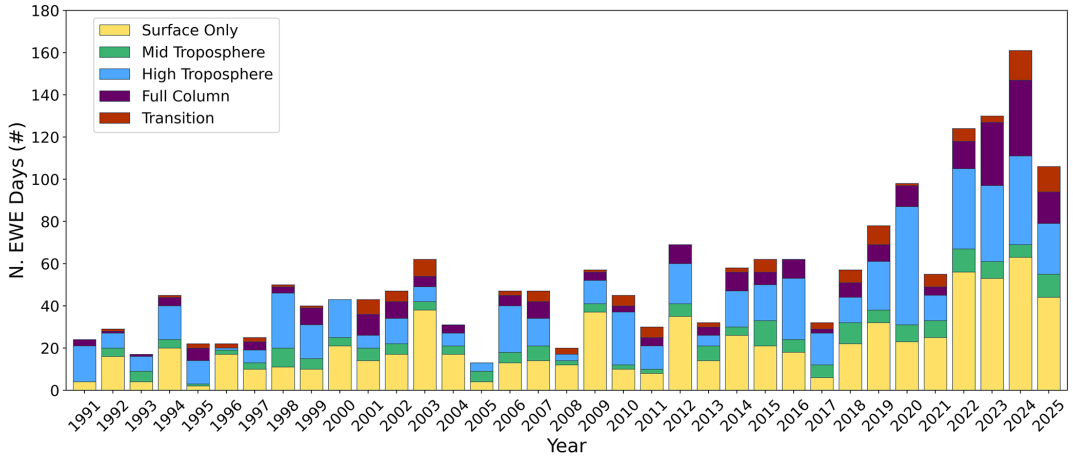

Figure 2. Timeseries of the EWE days divided into the five vertical categories described in Table 1. Annual frequency and vertical category distribution of EWE days over Rome from 1991 to 2025. Stacked bars represent the total annual count of EWE days, color-coded by the five categories defined in Table 1: *Surface Only* (yellow), *Mid Troposphere* (green), *High Troposphere* (cyan), *Full Column* (purple), and *Transition* (red).

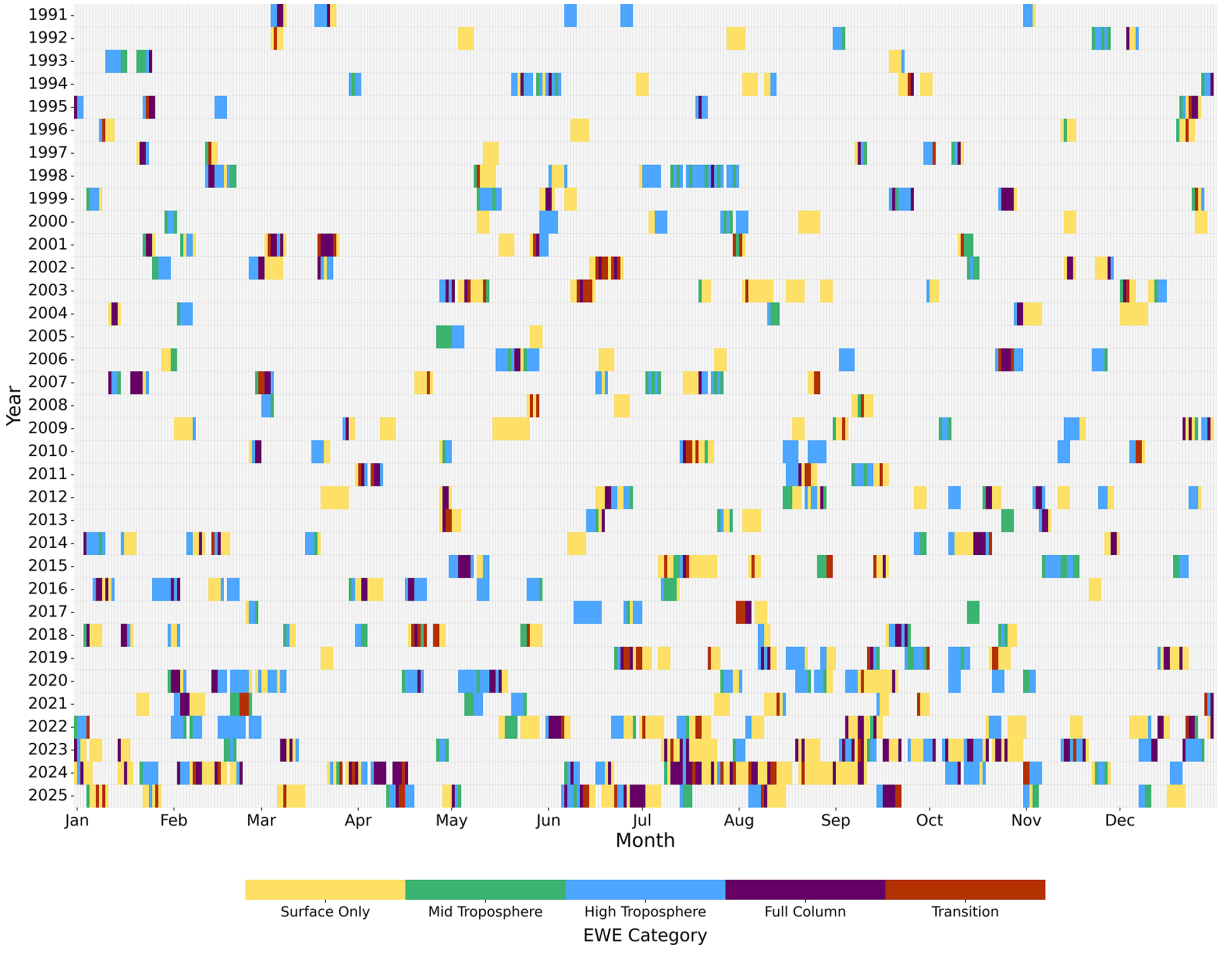

Figure 3. Multi-decadal distribution and occurrence of EWE days over Rome from 1991 to 2025. The x-axis shows the calendar timeline across all 12 months (January–December) versus years on the vertical axis. Coloured segments denote individual EWE days, color-coded by the five categories defined in Table 1: *Surface Only* (yellow), *Mid Troposphere* (green), *High Troposphere* (cyan), *Full Column* (purple), and *Transition* (red).

events, representing vertically coupled warm structures sustained by large-scale subsidence and surface radiative heating. Multi-decadally, Fig. 3 suggests an increase in overall event occurrence, and structural complexity during the most recent decade (particularly from 2015 to 2025). Alongside the higher occurrence of peak-summer *Full Column* and *Transition* events, the distribution qualitatively points toward an apparent seasonal extension, with *Surface Only* and *High Troposphere* EWEs appearing more frequently in shoulder months such as May, September, and October, as well as sporadically in winter. Future work will focus on the quantitative assessment of the statistical significance of these results, including the adoption of specific non-parametric tests for seasonal trends and change-point detection, such as the Seasonal Mann-Kendall test (Hirsch and Slack, 1984) and Pettitt's test (Pettitt, 1979).

3.3 Vertical structure and multi-level classification of Extreme Warm Regimes (EWRs)

To objectively categorize the diverse atmospheric structures associated with EWEs over Rome, a K-means clustering analysis was performed using temperature anomalies at 1000, 500, and 300 hPa. The combined application of the Elbow Method and the Silhouette Analysis identified five clusters as the optimal partition of the dataset (Fig. A1), composed of a total of 1371 d. Each cluster represents a distinct vertical thermodynamic structure, hereafter referred to as an EWR.

The mean vertical profiles of thermal anomalies ΔT, obtained by averaging all days assigned to each cluster, are shown in Fig. 4 and reveal substantial variability in the vertical distribution and intensity of atmospheric warming. Expressing these profiles in terms of ΔT provides a direct measure of thermal energy content throughout the column, while altitude-dependent differences in temperature variance are implicitly controlled for during event identification through level-specific percentile thresholds. Furthermore, the spread depicted by the shaded regions (± 1 standard deviation σ_{T_p}) reflects the natural intra-regime variability: while deep coupled regimes show strong structural consistency due to dominant synoptic subsidence, elevated and decoupled classes display wider dispersion owing to fluctuations in the exact core altitude and amplitude of upper-level features across seasons. The detailed structural properties of each regime are as follows:

i. *Extreme Deep* (n days $= 294$): the strongest and most vertically coupled EWR, characterized by intense warming throughout the tropospheric column. Temperature anomalies exceed 6 °C in the middle troposphere and remain strongly positive at all analysed pressure levels, indicating a highly coupled warm structure extending from the lower to the high troposphere;

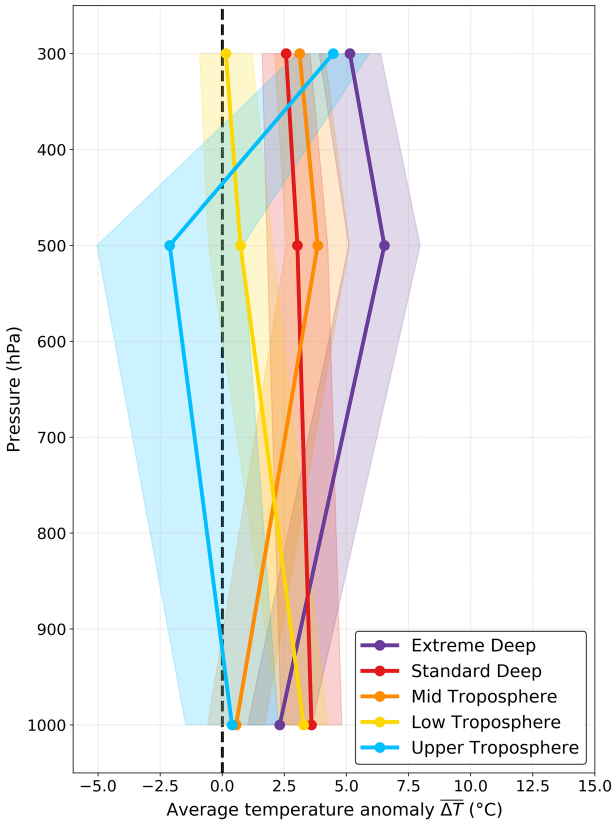

Figure 4. Vertical profiles of thermal anomalies $\overline{\Delta T}$, obtained by averaging profiles of all days belonging to each EWR. Horizontal shaded regions depict ± 1 standard deviation σ_{T_p}.

ii. *Standard Deep* (n days $= 553$): a vertically consistent warming profile with temperature anomalies of approximately 3–4 °C. This regime represents a moderate-intensity deep-warming configuration affecting most of the tropospheric column;

iii. *Mid Troposphere* (n days $= 529$): warming reaches its maximum in the middle troposphere (500 hPa), while anomalies progressively weaken toward both the surface and upper atmospheric levels. This pattern indicates a partially decoupled vertical structure, with anomalous heating concentrated primarily in intermediate layers;

iv. *Low Troposphere* (n days $= 459$): temperature anomalies peak near the surface (about 3.0 °C) and decrease as the altitude increases. The resulting profile suggests a warm structure largely confined to the lower troposphere, with limited extension into the free atmosphere;

v. *Upper Troposphere* (n days $= 65$): a highly stratified thermal profile, where anomalies are negligible at the surface but exceed 4.5 °C at 300 hPa. These relatively infrequent events are likely associated with high tropo-

sphere dynamical perturbations or Rossby-wave activity with limited coupling to the lower troposphere.

The physical consistency of the clustering framework is further supported by Fig. A2, which shows the relative contribution of the EWE categories introduced in Sect. 3.2 within each statistically derived EWR. Among all EWRs, the *Extreme Deep* regime exhibits the largest percentage of EWEs classified as *Full Column*, highlighting that the most intense events are typically associated with vertically coupled warming throughout most of the tropospheric column. Similarly, the *Standard Deep* regime includes substantial contributions from *Surface Only* and *Full Column* EWEs, suggesting a mixed regime where both lower-tropospheric thermodynamic feedback and large-scale subsidence contribute to development of EWEs. The *Mid Troposphere* regime is primarily associated with *High Troposphere* and *Low Troposphere* categories, highlighting the prevalence of vertically decoupled atmospheric configurations. Conversely, the *Low Troposphere* regime is almost entirely associated with *Surface Only* events, reinforcing its interpretation as a shallow, PBL-confined EWR. Finally, the *Upper Troposphere* regime is overwhelmingly dominated by *High Troposphere* events, confirming that these cases remain largely confined to upper atmospheric levels.

To characterize the large-scale atmospheric configurations associated with each EWR, Fig. 5 shows the ERA5 composite maps of geopotential height at 500 hPa, Z_{500}, and temperature anomaly at 850 hPa, ΔT_{850}, averaged across all days belonging to each specific EWR. Although all regimes are associated with positive thermal anomalies over the central Mediterranean, substantial differences emerge in their spatial organization and vertical structure.

The *Extreme Deep* EWR is associated with a pronounced Z_{500} ridge centred over the central Mediterranean and extending across much of southern Europe (Fig. 5a). Although the ΔT_{850} maximum is slightly displaced toward central-western Mediterranean, the overall structure suggests intense subsidence-driven warming and an efficient vertical propagation of thermal anomalies throughout the atmospheric column. The *Standard Deep* EWR presents a similar anomaly structure. Z_{500} peaks over the Central Mediterranean, while the temperature anomaly field exhibits a maximum (up to +6 °C) over Italy (Fig. 5b), consistent with combined contributions from warm-air advection and large-scale subsidence. The *Mid Troposphere* EWR is characterized by a ridge configuration, with maximum ΔT_{850}confined over North Africa and the western Mediterranean (Fig. 5c). This configuration is consistent with atmospheric conditions in which warming is experienced in intermediate tropospheric layers without the development of a fully coupled deep-column structure. The *Low Troposphere* EWR presents a synoptic configuration similar to that of the *Standard Deep* regime (Fig. 5d). In this case, ΔT_{850} assumes the highest value over Italy (about +6 °C), suggesting predominantly shallow warm

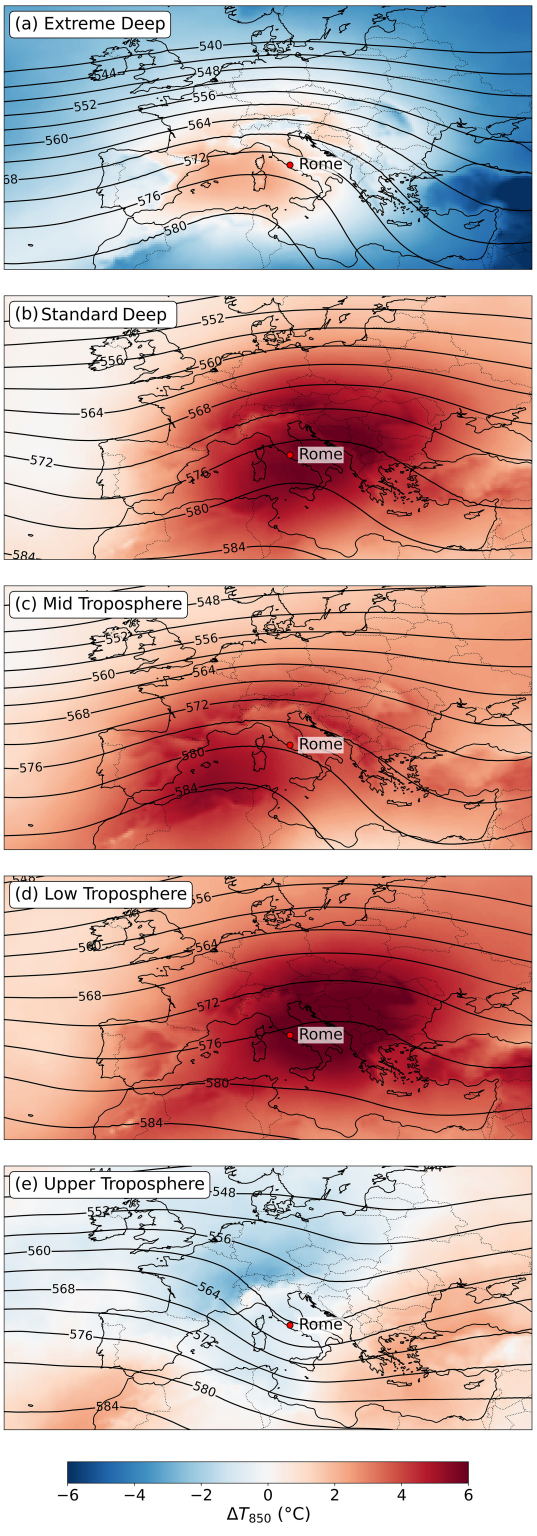

Figure 5. ERA5 composite maps for the five EWRs identified: **(a)** *Extreme Deep*, **(b)** *Standard Deep*, **(c)** *Mid Troposphere*, **(d)** *Low Troposphere*, and **(e)** *Upper Troposphere*. Panels depict geopotential height at 500 hPa (Z_{500}, solid black contours, in dam) overlaid on mean air temperature anomalies at 850 hPa (ΔT_{850} colour shaded, in °C). ERA5 data © Copernicus Climate Change Service (C3S), ECMWF.

advection and enhanced PBL heating rather than intense free-tropospheric subsidence. In contrast, the *Upper Troposphere* EWR exhibits the weakest surface signature among all EWRs (Fig. 5e). The ΔT_{850} field remains close to climatological conditions over Italy, indicating that the thermal anomalies identified in the vertical profiles are confined to upper atmospheric levels and likely associated with transient jet-stream perturbations or Rossby-wave activity. To further assess whether the driving mechanisms and spatial characteristics of EWRs depend on the seasonal cycle, independent seasonal composite maps were constructed for the four meteorological seasons (Figs. A3–A6). This seasonal analysis reveals that the core synoptic configurations and vertical decoupling mechanisms identified in the annual baseline remain physically robust across all seasons, confirming that the identified EWRs represent recurring atmospheric modes rather than artifacts of seasonal aggregation. In particular:

- Coupled Regimes (*Extreme Deep* and *Standard Deep* EWRs): across all seasons, both coupled regimes are consistently governed by high-amplitude upper-level ridges driving strong lower-tropospheric warm advection ($\Delta T_{850} > 4\,°C$) and subsidence heating. During winter (Fig. A6a and b) and spring (Fig. A3a and b), these regimes manifest as prominent blocking patterns or high-amplitude subtropical ridges steering tropical air masses towards Central Europe. In summer (Fig. A4a and b), geopotential gradients are broader and less intense, but positive thermal anomalies remain strong and geographically focused over the Central Mediterranean.

- Decoupled Regimes (*Mid Troposphere*, *Low Troposphere*, and *Upper Troposphere*): the intensity and characteristics of vertical decoupling exhibit distinct seasonal signatures. During summer and autumn, the *Mid Troposphere* EWR (Figs. A4c and A5c) shows marked thermal decoupling, where elevated warm anomalies coincide with near-neutral or slightly negative lower-tropospheric anomalies over the Mediterranean basin, linked to transient troughs and baroclinic activity. Conversely, the *Low Troposphere* EWR (Figs. A4d and A5d) consistently retains strong surface-bound warming ($\Delta T_{850} > 2\,°C$) under relatively zonal or weak upper-level flow, emphasizing boundary-layer thermodynamic processes irrespective of season. Finally, the *Upper Troposphere* regime (Figs. A3e–A6e) is persistently associated with high-tropospheric ridge axes and tropopause displacements, reaching its strongest spatial coherence during summer and autumn (Figs. A4e and A5e).

Overall, the composite analysis indicates that the statistically derived EWRs correspond to physically meaningful atmospheric configurations rather than purely statistical partitions of the dataset, thereby providing a synoptic-scale interpretation of the vertical thermal structures identified by the clustering analysis.

The temporal evolution of the EWR metrics (Table 2) over the 1991–2025 period (Fig. 6) reveals substantial changes in the frequency and thermodynamic contribution of the different atmospheric configurations associated with EWEs over Rome.

The most evident signal emerges from the quinquennial evolution of the EWRs frequency (Fig. 6a), which shows a marked increase in the occurrence of all EWRs during the last decade, particularly after 2015. The strongest growth is observed for the *Standard Deep* and *Extreme Deep* regimes, whose combined frequency increases sharply during 2021–2025 and accounts for a large fraction of all identified EWR days. In contrast, the mean duration of individual episodes exhibits limited long-term variability (Fig. 6b). Although minor fluctuations are evident among quinquennia, average durations remain relatively stable across all EWRs, generally ranging between approximately 1.5 and 3.5 d. The *Mid Troposphere* and *Low Troposphere* EWRs consistently display slightly longer durations than the Deep EWRs, while the *Upper Troposphere* regime remains the shortest-lived configuration throughout the study period. Similarly, the mean column-averaged temperature anomaly associated with each EWR remains remarkably stable over time (Fig. 6c). The *Extreme Deep* regime consistently exhibits the highest column anomalies ($\sim 4.5\,°C$), followed by *Standard Deep* ($\sim 3\,°C$) and *Mid Troposphere* ($\sim 2.5\,°C$). Lower anomaly intensities characterize the *Low Troposphere* EWR, whereas the *Upper Troposphere* EWR displays greater temporal variability, including slightly negative column-averaged anomalies during 2001–2005 and 2006–2010. This behaviour is primarily driven by its very low sample size and its physical structure: since warm anomalies in this regime are strictly confined to 300 hPa, neutral or slightly cooler-than-average conditions in the lower and mid-troposphere can result in a marginally negative value when averaged across the entire vertical column. A different behaviour emerges from the evolution of the CHI metric (Fig. 6d). The largest CHI values are consistently associated with the *Extreme Deep* EWR, followed by *Standard Deep* and *Mid Troposphere*. The CHI time series reveals pronounced multi-decadal variability. While the cumulative annual number of days belonging to deep, vertically coupled regimes (e.g., *Extreme Deep*) has increased post-2000, the intrinsic intensity (CHI) of individual events within these regimes exhibits strong decadal fluctuations rather than a uniform upward trend. This non-monotonic behaviour underscores that recent shifts in integrated thermal load reflect the combined effect of warming trends and internal atmospheric variability, such as low-frequency synoptic circulation patterns and decadal blocking persistence, rather than a simple linear acceleration in event severity.

Overall, these results suggest that the recent intensification of EWEs over the study area is primarily linked to the

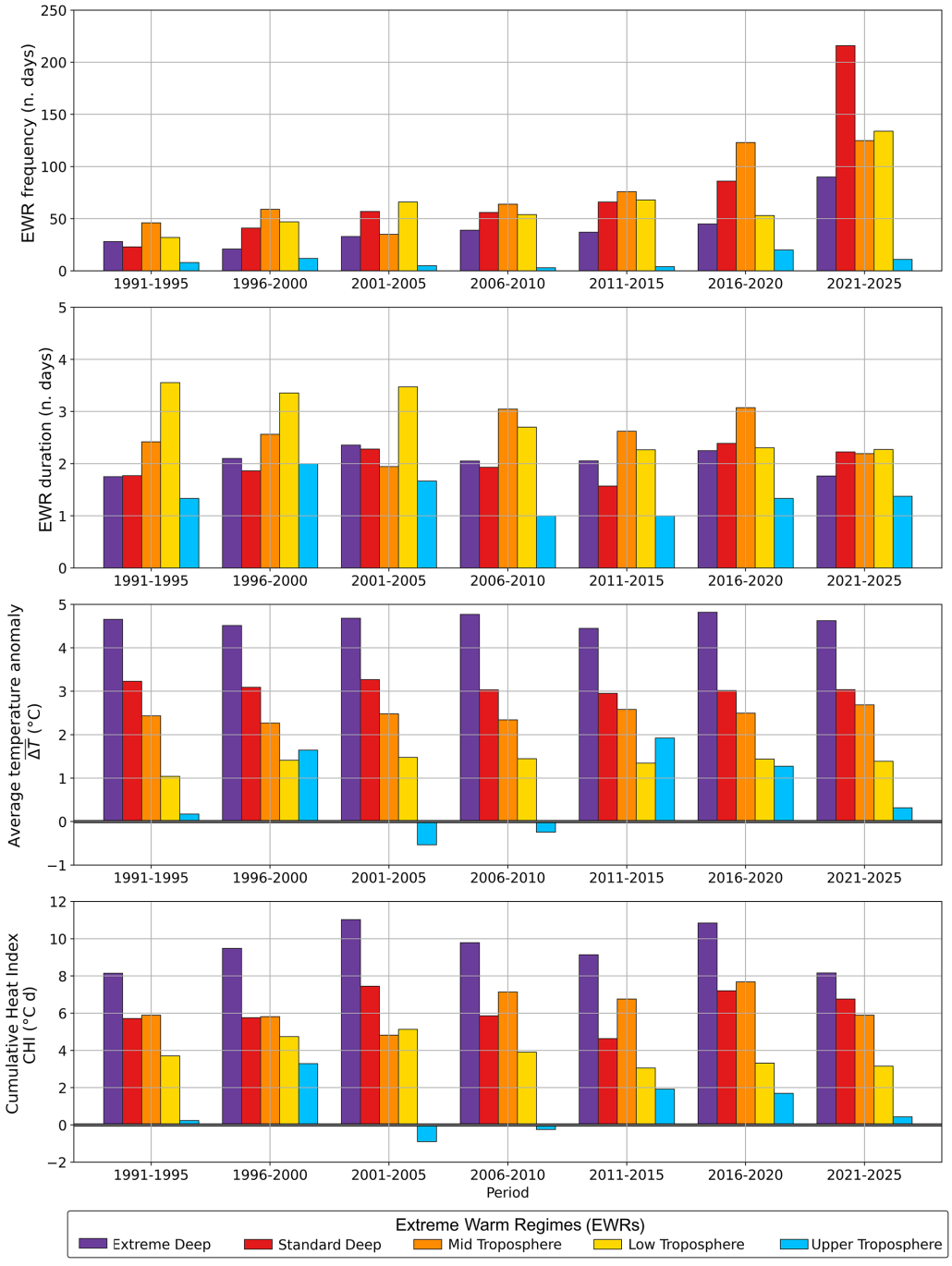

Figure 6. Quinquennial variability of EWR metrics across the five identified clusters for the period 1991–2025.

increasing occurrence of Deep EWRs rather than to systematic changes in their duration or mean thermal intensity.

To investigate the dynamic mechanisms and vertical structures driving the onset of the different atmospheric configurations and quantify their inter-event spread, Fig. 7 depicts the temporal evolution of cluster-averaged temperature anomalies $\overline{\Delta T_p(t)}$ at 1000, 500, and 300 hPa from 3 d prior to the event (t_{-3}) up to the onset day (t_0), with vertical error bars representing ± 1 standard deviation across events within each EWR. This lagging framework highlights the distinct precursory pathways, vertical coupling modes, and intra-regime variability characterizing each extreme regime.

All EWRs exhibit a shared behaviour in the upper atmospheric layers during the earliest precursor phase (t_{-3} to t_{-2}), where the upper (300 hPa) and mid troposphere (500 hPa) track each other closely, displaying well-defined, parallel

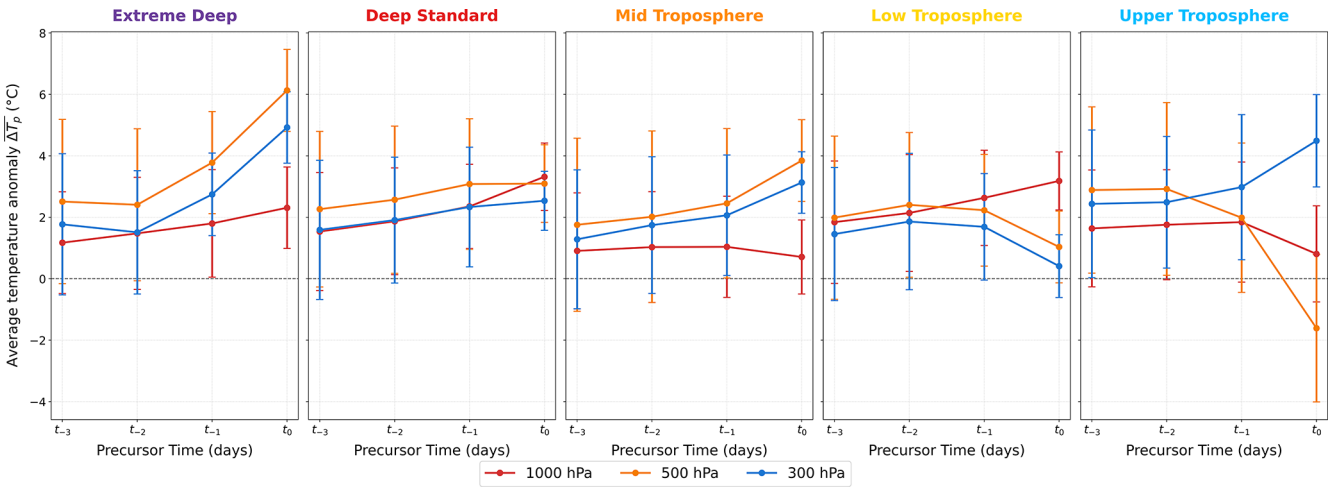

Figure 7. EWR-averaged thermal anomalies ($\overline{\Delta T_p}$) computed over the 4 d precursor temporal window for the five identified EWRs. The temporal evolutions refer to 1000 hPa (red lines), 500 hPa (orange lines), and 300 hPa (blue lines). The dashed black horizontal line depicts the zero-anomaly climatological baseline. Solid lines show composite mean values, while vertical error bars denote ±1 inter-event standard deviation, illustrating intra-regime spread.

warm anomalies ranging between +1.2 and +3.0 °C. This widespread high troposphere initialization confirms that the vast majority of EWEs over the region possess a distinct free-tropospheric signature well before appearing at the surface. However, their evolutionary pathways structurally diverge as the onset approaches. Specifically, for the *Extreme Deep* EWR, a powerful top-down intensification mechanism occurs as t_0 approaches; the mid-tropospheric warm core surges abruptly from t_{-2} onward, with the 500 hPa anomalies exceeding +6.0 °C at t_0, while the 300 hPa layer reaches approximately +5.0 °C. Conversely, the lowest tropospheric layer (1000 hPa) undergoes a steady but more gradual warming, reaching +2.3 °C at t_0. This behavior demonstrates that these severe events are initiated by macro-scale synoptic ridging and intense adiabatic compression under strong subsidence, which progressively forces the thermal anomaly downward until full vertical alignment is achieved at t_0. The *Standard Deep* EWR presents a similar but more moderate top-down development, where all three levels converge symmetrically at t_0 within a modest anomaly range of +2.5–3.5 °C. The *Mid Troposphere* EWR exhibits a remarkable thermodynamic decoupling of the surface layer throughout the precursor window. This is evidenced by the contrasting evolution of the vertical temperature anomalies: from t_{-3} to t_{-1}, the 300 and 500 hPa levels show a progressive increase in their warm anomalies, whereas the near-surface layer remains stationary or drops slightly toward the climatological baseline (around +0.7 °C). This pattern indicates that the precursory warming is initially confined to the free atmosphere, likely associated with elevated warm advection or persistent high troposphere ridging that has not yet coupled with the PBL. In stark contrast to the top-down regimes, the *Low Troposphere* EWR is driven by a clear bottom-up warming. At t_{-3} and t_{-2}, the entire tropospheric column appears moderately and homogeneously warm (+1.5–2.5 °C). From t_{-1} onward, however, the vertical structure undergoes a radical stratification: the mid and high troposphere undergo a rapid cooling trend, dropping to +1.0 °C (500 hPa) and +0.4 °C (300 hPa) at t_0. Conversely, a localized thermal intensification occurs exclusively near the surface, with the 1000 hPa anomaly climbing steadily to exceed +3.2 °C at t_0. This upper-level cooling reflects the eastward displacement of upper-level ridge support and the passage of weak baroclinic perturbations aloft, which effectively strip the free atmosphere of warm anomalies while trapping sensible heat and local advective fluxes within a shallow, PBL-confined layer near the surface. Finally, the *Upper Troposphere* EWR represents a highly isolated, high-altitude extreme structure. Throughout the precursor window, the 300 hPa level maintains a steadily increasing warm anomaly that reaches +4.5 °C at t_0. In contrast, the mid and lower troposphere display a striking downward trend. At t_0, the vertical decoupling across the column becomes pronounced. Indeed, the high troposphere reaches its thermal peak, the near-surface anomaly drops below +1.0 °C, and the mid-troposphere undergoes a prominent collapse, falling well below the climatological baseline to approximately −1.6 °C. Dynamically, this contrasting vertical dip at 500 hPa paired with intense heating at 300 hPa is characteristic of upper-level wave-breaking and local tropopause folding. The extreme thermal anomaly remains rigidly confined to the upper troposphere, while an influx of cooler baroclinic air in the mid-troposphere prevents vertical propagation toward the surface.

The vertical spread depicted by the error bars demonstrates that while individual events vary in absolute magnitude (≈ 1.5–2.5 °C), the mean temperature evolutions con-

sistently lie well within ±1 standard deviation of the event population, confirming that the overarching precursory trajectories and layer-specific decoupling trends remain structurally consistent across individual episodes.

3.4 Spatiotemporal characterization of case studies

To illustrate the physical mechanisms and thermodynamic pathways associated with the statistically derived EWRs, one representative event was selected for each cluster following the criteria detailed in Sect. 2.7. The selected episodes maximize the CHI values while preserving the dominant EWE category associated with each regime (Table 4).

Together, the time-height cross-section of ΔT and θ_e (Fig. 8), the corresponding synoptic configurations, and the HYSPLIT backward trajectories (Fig. 9) provide a process-based diagnostic illustration of the physical mechanisms governing each EWR. In Fig. 8, the vertical progression of the signals is identified through the temporal evolution and time-height tilt of these anomaly contours and θ_e isolines across pressure levels; specifically, a contour slope extending downward over time indicates downward development, whereas an opposite slope highlights upward propagation.

The *Extreme Deep* case (19–22 January 2007) is characterized by exceptionally strong mid-tropospheric warming, with mean anomalies reaching +8.25 °C at 500 hPa, decreasing to +5.84 °C at 300 hPa, while remaining positive near the surface ($\overline{\Delta T_{1000}} = +3.24$ °C; Table 4). The time-height evolution (Fig. 8a) indicates that warming first intensifies above approximately 600–700 hPa and progressively propagates downward over the following days, leading to the development of a vertically coupled warm anomaly. Throughout the event, θ_e exhibits only limited temporal variability and does not develop a pronounced elevated maximum (Fig. 8b), suggesting that the event is not associated with a substantial increase in the thermodynamic content of the atmospheric column. This interpretation is supported by the large-scale circulation, which is dominated by a compact blocking anticyclone over the central Mediterranean (Fig. 9a), while the backward trajectories reveal descending continental air masses arriving over Rome from the European sector (Fig. 9b). The close agreement between the vertical thermal evolution, the synoptic configuration and the transport pathways indicates that this winter event is primarily sustained by persistent subsidence and adiabatic compression rather than by long-range warm-air advection.

The *Standard Deep* event (2–5 June 2022) also evolves toward a vertically coupled warm column, although within a substantially different thermodynamic environment. Even if positive anomalies extend throughout the atmospheric column, the largest warming is concentrated in the lower troposphere, where $\overline{\Delta T_{1000}}$ reaches +6.11 °C, while anomalies remain close to +3.50 °C at both 500 and 300 hPa (Table 4). Unlike the winter case, the θ_e field evolves rapidly after the onset, developing a pronounced maximum within the middle troposphere (Fig. 8d), indicative of a progressive increase in the thermodynamic content of the air mass. At the synoptic scale, the event coincides with a broad subtropical ridge extending from North Africa across the central Mediterranean (Fig. 9c). Consistently, the HYSPLIT trajectories trace the lower-to-mid tropospheric air parcels back to North Africa after crossing the Mediterranean Sea (Fig. 9d), highlighting the significant contribution of subtropical air-mass advection to the development of the vertically coupled warm structure. In contrast to the winter *Extreme Deep* case, the *Standard Deep* event develops under much stronger advective forcing, producing the strongest lower-tropospheric warming among the five representative events. Despite their contrasting seasonal environments, both events evolve toward a vertically coupled warm column, supporting the interpretation that the Deep EWRs represent dynamically coupled atmospheric structures, although sustained by different large-scale processes.

In contrast, the remaining three case studies are characterized by persistent vertical decoupling, although the altitude at which the thermal anomaly develops differs substantially among the regimes.

The *Mid Troposphere* case (3–12 May 2020) illustrates a vertically decoupled configuration in which warming remains largely confined to the free troposphere. Mean temperature anomalies reach +3.43 °C at 500 hPa and +4.08 °C at 300 hPa, whereas the lower troposphere experiences only weak warming (+0.35 °C at 1000 hPa; Table 4). The time-height evolution (Fig. 8e) shows that the warm core remains centred between approximately 800 and 400 hPa for most of the event, with only limited downward propagation towards the lowest portion of the troposphere. A comparable vertical organization is evident in the θ_e field (Fig. 8f), where the highest values persist aloft while the lower troposphere undergoes only modest temporal variations, suggesting that the thermodynamic anomaly remains largely confined to the free atmosphere. This behaviour is consistent with the synoptic configuration (Fig. 9e), which places Rome along the northern flank of a subtropical ridge extending across North Africa and the western Mediterranean. The backward trajectories further support this interpretation (Fig. 9f), showing that the upper-level air parcels remain elevated throughout their transport, whereas the lower-level trajectories are comparatively short and predominantly regional. The persistence of this vertically decoupled structure closely matches the precursor evolution identified in Sect. 3.3, confirming that the anomalous warming remains dynamically confined to the free troposphere throughout the event.

The *Low Troposphere* event (1–9 December 2004) is characterized by warming almost entirely confined up to 950 hPa. The strongest anomalies occur near the surface, reaching +3.65 °C at 1000 hPa, while they rapidly decrease with height (+1.85 °C at 500 hPa) and become slightly negative at 300 hPa (−0.31 °C; Table 4). The time-height evolution (Fig. 8g) shows that the positive anomaly remains largely

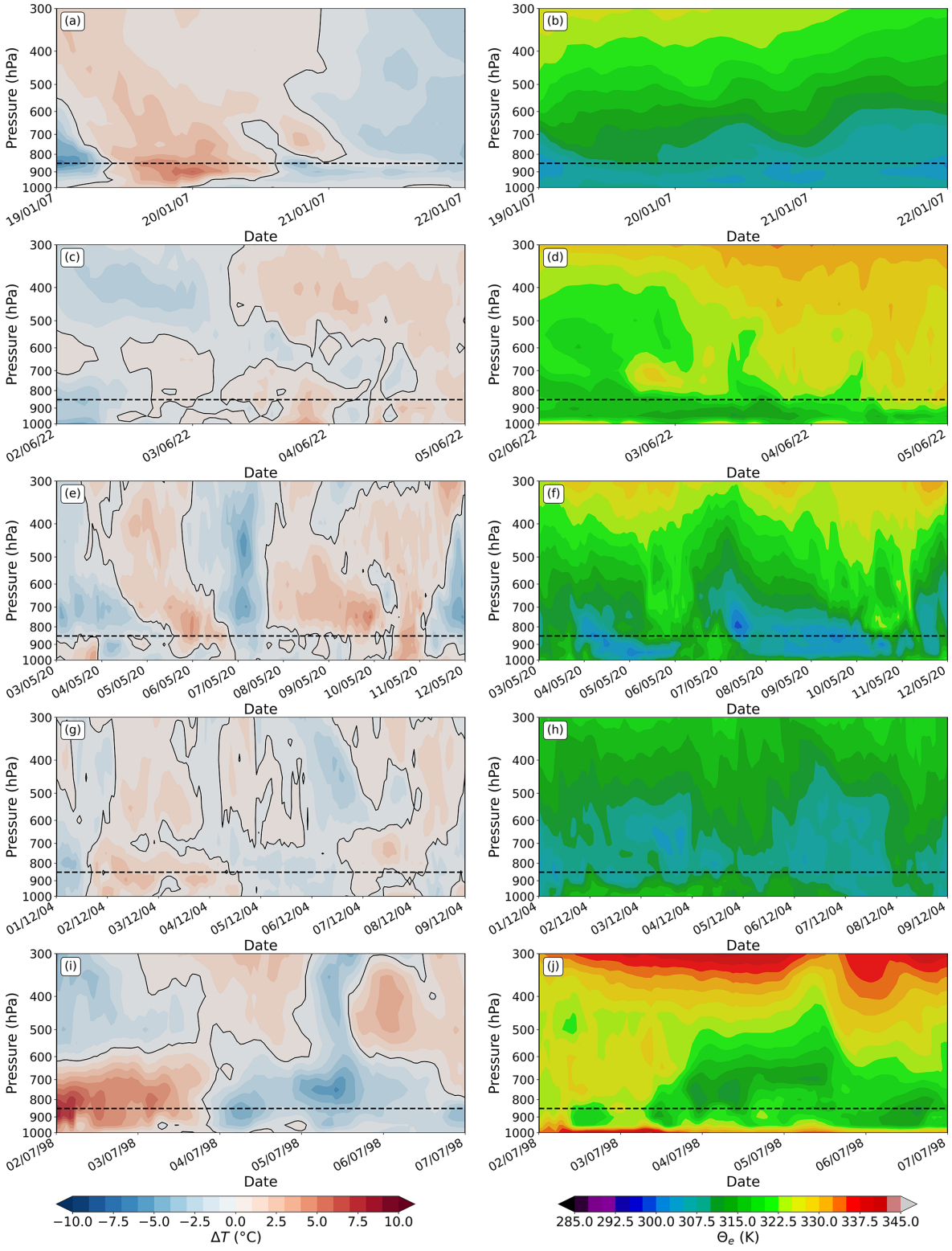

Figure 8. Time-height cross-sections of the selected case studies. Left panels: temperature anomalies (ΔT, in °C) calculated relative to the 21 d local climatological window, with solid black contours denoting the 0.0 °C anomaly line. Right panels: equivalent potential temperature (θ_e, in K). From top to bottom, rows correspond to the identified EWRs: *Extreme Deep*, *Standard Deep*, *Mid Troposphere*, *Low Troposphere*, and *Upper Troposphere*. Horizontal, black dashed line refers to the 850 hPa level shown in the composite maps in Fig. 9. Note that in each panel the onset time of the event (t_0) corresponds to the start of the time axis in each panel and that the duration displayed on the x-axis corresponds to the full lifecycle of each specific event, ranging from 4 d **(a–d)** up to 10 d **(e, f)**.

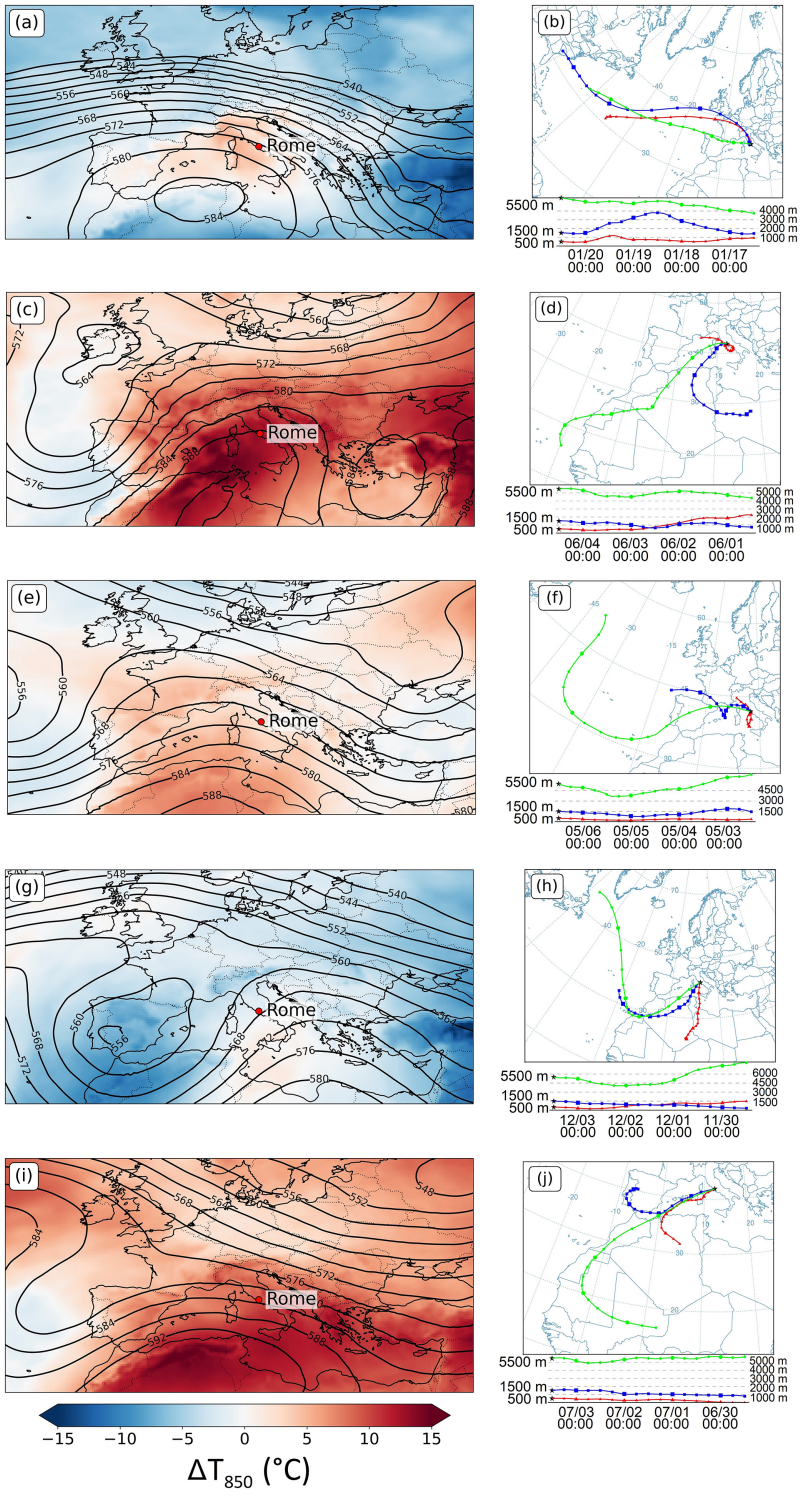

Figure 9. Spatial synoptic characterization and 144 h HYSPLIT backward trajectories for the selected case studies, organized by EWRs from top to bottom: **(a, b)** *Extreme Deep*, **(c, d)** *Standard Deep*, **(e, f)** *Mid Troposphere*, **(g, h)** *Low Troposphere*, and **(i, j)** *Upper Troposphere*. Left panels: ERA5 composite maps of geopotential height at 500 hPa (Z_{500}, gpm, black solid lines) and temperature anomaly at 850 hPa (T_{850}, °C, color shading) averaged over the respective event duration. Right panels: 144 h HYSPLIT backward trajectories arriving over Rome at 12:00 UTC on the day of maximum thermal anomaly. Spatial tracks illustrate air mass movement from remote origins toward Rome, with arrival altitudes set at 500 m (red lines), 1500 m (blue lines), and 5500 m (green lines) above ground level (agl). Bottom sub-panels display the corresponding vertical displacement profiles backward in time from the arrival date (t_0) on the left back to t_{-144} on the right. ERA5 data © Copernicus Climate Change Service (C3S), ECMWF. HYSPLIT model data by NOAA Air Resources Laboratory.

Table 4. Summary of the representative case studies selected for each EWR. For each event, the dominant EWE category, period of occurrence, total duration, mean temperature anomalies at the three reference pressure levels ($\overline{\Delta T_{1000}}$, $\overline{\Delta T_{500}}$, and $\overline{\Delta T_{300}}$), and the Cumulative Heat Index (CHI) are reported.

EWR category	EWE category	EWE Period	Duration (n days)	$\overline{\Delta T_{1000}}$ (°C)	$\overline{\Delta T_{500}}$ (°C)	$\overline{\Delta T_{300}}$ (°C)	CHI (°C d)
Extreme Deep	*Full column*	19—22 January 2007	4	3.24	8.25	5.84	69.32
Standard Deep	*Full column*	2–5 June 2022	4	6.11	3.30	3.61	52.10
Mid Troposphere	*High troposphere*	3–12 May 2020	10	0.35	3.43	4.08	72.29
Low Troposphere	*Surface only*	1–9 December 2004	9	3.65	1.85	-0.31	43.72
Upper Troposphere	*High Troposphere*	2–7 July 1998	6	0.01	0.92	4.87	23.48

confined below approximately 600 hPa throughout the event. Unlike the Deep regimes, the θ_e field (Fig. 8h) displays relatively weak vertical organization, without the development of an elevated thermodynamic maximum in the free troposphere. At the synoptic scale, the event is associated with the transition from a high- to low- pressure system over the central Mediterranean (Fig. 9g), accompanied by only modest positive temperature anomalies at 850 hPa, suggesting that large-scale dynamical forcing provides only a limited background contribution. Consistently, the HYSPLIT trajectories (Fig. 9h) indicate predominantly short transport pathways with little vertical displacement before reaching Rome. Together, these features indicate that the thermal anomaly is primarily generated and maintained within the PBL, with only limited interaction with the overlying free atmosphere.

The *Upper Troposphere* event (2–7 July 1998) represents a pronounced example of persistent upper-level warming without effective coupling to the lower troposphere. The strongest anomalies remain confined to the upper atmospheric layers, where the mean temperature anomaly reaches +4.87 °C at 300 hPa, while the lower troposphere remains close to climatological conditions ($\overline{\Delta T_{1000}} = +0.01$ °C) and only weak warming develops at mid-levels ($\overline{\Delta T_{500}} = +0.92$ °C, Table 4). The time-height evolution (Fig. 8i) shows that the warm anomaly is initially restricted above approximately 500 hPa and only marginally extends downward during the later stages of the event, without establishing a vertically coupled structure. The θ_e field exhibits a comparable evolution (Fig. 8j), with its largest values persistently located in the upper troposphere and only limited temporal variability within the PBL, further highlighting the strong vertical separation between the upper and lower atmosphere. The associated synoptic configuration (Fig. 9i) is characterized by a broad subtropical ridge centred over North Africa, while the strongest low-level thermal anomalies remain displaced south of the central Mediterranean. Likewise, the backward trajectories (Fig. 9j) show that only the highest air parcels originate from subtropical latitudes and remain aloft throughout their transport, whereas the lower-level trajectories remain comparatively local and experience minimal vertical displacement. The close correspondence between the vertical thermal evolution, the synoptic configuration, and the transport pathways exemplifies how the anomalous warming remains effectively isolated within the upper troposphere, preventing the establishment of the vertically coupled warm column that characterizes the Deep EWRs.

4 Discussion

The results highlight a substantial change not only in the frequency of EWEs but also in their vertical thermodynamic structure.

Although the increase in EWE frequency aligns with broader Mediterranean climate change trends (Perkins-Kirkpatrick and Lewis, 2020; Seneviratne et al., 2021; Rousi et al., 2022), the present multi-level framework demonstrates that this increase is not homogeneous across the different EWRs. The strongest rise is associated with vertically coupled regimes (*Full Column* and *Standard Deep* EWRs), suggesting that large-scale dynamical forcing is playing a progressively greater role in shaping Mediterranean heat extremes than shallow, near-surface processes alone.

This interpretation is consistent with the long-term temporal trends identified throughout the tropospheric column. The pronounced positive trends observed during summer and autumn suggest a seasonal stretching of summer-like atmospheric configurations, likely associated with increased persistence and expansion of subtropical ridging over the Mediterranean basin (Cramer et al., 2018; Cos et al., 2022). This behaviour agrees with previous studies linking Mediterranean warming to large-scale circulation changes and enhanced atmospheric blocking weather patterns (Giannakopoulos et al., 2009; Molina et al., 2020; Zittis et al., 2021).

Combining clustering, precursor analysis, and case studies, the five EWRs can be grouped into two main dynamical classes:

- Coupled events (*Extreme Deep* and *Standard Deep EWRs*): both regimes evolve toward a vertically coherent warm column, but through partly different pathways. As the ridge deepens, intense synoptic-scale subsidence and adiabatic compression force the warm

anomaly downward until full vertical alignment is achieved at the EWE onset, overriding local mitigating factors (Lhotka et al., 2018; Sousa et al., 2018; Zschenderlein et al., 2019). The *Extreme Deep* precursor is characterized by the progressive downward extension of a mid-tropospheric warm anomaly, consistent with persistent blocking, subsidence, and adiabatic warming, as documented in recent process-based Lagrangian frameworks (Röthlisberger and Papritz, 2023; Hotz et al., 2024). In contrast, the *Standard Deep* regime develops within a subtropical ridge and is accompanied by low-level warm-air advection from North Africa, favouring rapid warming of the lower troposphere and the establishment of a vertically coupled atmospheric structure. Despite these differences, both regimes ultimately evolve toward a fully coupled tropospheric column dominated by large-scale forcing and mid-tropospheric warming signatures often associated with Rossby wave breaking (Fix-Hewitt et al., 2026a; Hotz et al., 2026).

– Decoupled events (*Mid Troposphere*, *Low Troposphere*, and *Upper Troposphere* EWRs): unlike the Deep EWRs, these events never develop a vertically coupled warm column. Instead, the thermal anomaly remains confined to a limited portion of the troposphere, indicating that the large-scale forcing is either insufficient or unable to establish effective vertical coupling. In the *Mid Troposphere* case, the anomaly is confined to the free troposphere throughout the event, indicating limited penetration toward the PBL. The *Low Troposphere* EWR shows the opposite behaviour, with warming restricted to the PBL and weak anomalies aloft, mainly attributable to surface-driven processes, such as enhanced sensible heat fluxes, shallow warm advection, and local land-atmosphere feedback (Seneviratne et al., 2010; Stéfanon et al., 2014; Hirsch and King, 2020; Röthlisberger and Papritz, 2023). The *Upper Troposphere* EWR remains isolated in the higher troposphere, likely associated with transient upper-level dynamical disturbances that do not project onto the surface (Fix-Hewitt et al., 2026b; Hotz et al., 2026). Together, these cases mirror the spectrum of three-dimensional thermal configurations recently identified in regional reanalyses (Fix-Hewitt et al., 2026a), confirming that strong warming aloft does not necessarily translate into near-surface extremes.

It is worth noting that the physical mechanisms identified here, such as synoptic compression, subsidence, and subtropical warm-air advection, are fundamental atmospheric processes not strictly unique to the Central Mediterranean. Rather, what characterizes this region is the specific interplay between large-scale upper-level ridging, intense continental or African warm advection, and local coastal/marine boundary layer dynamics.

The increasing frequency of Deep EWRs has relevant implications for Mediterranean coastal cities. Under typical summer conditions, sea-breeze circulations can mitigate daytime heat by importing cooler marine air inland (Bedoya-Valestt et al., 2026). During Deep events, however, the persistence of large-scale warming throughout much of the tropospheric column may weaken these mesoscale cooling mechanisms. Although sea-breeze dynamics are not explicitly resolved here, the synoptic patterns suggest conditions less favourable to their development, with strong anticyclonic control and reduced pressure gradients. This may enhance the persistence of heat over coastal urban areas such as Rome.

Several limitations of the present study must, however, be recognized. First, the analysis relies on ERA5 reanalysis data, which lacks the horizontal resolution necessary to explicitly resolve fine-scale urban canopy dynamics, UHI, or complex mesoscale coastal circulations. Moreover, a key limitation of utilizing a 35-year reanalysis dataset is the difficulty in isolating anthropogenic climate trends from natural, low-frequency atmospheric fluctuations, such as shifts in the Atlantic Multidecadal Variability (AMV) or the North Atlantic Oscillation (NAO). Consequently, the increase in vertically coupled regimes observed after 2000 should be interpreted with caution. Moreover, a higher occurrence of coupled thermodynamic profiles does not directly translate into an increase in the frequency or duration of atmospheric blocking events. Verifying whether blocking structures are becoming inherently more persistent would require dedicated kinematic blocking detection algorithms across the broader Euro-Atlantic domain, which falls outside the scope of local vertical temperature analysis. Second, the multi-level clustering framework is inherently sensitive to the choice of the specific pressure levels (1000, 500, and 300 hPa) and the threshold utilized for EWE identification. While adopting a stricter threshold would naturally isolate rarer and more severe events, the 90th percentile was selected to maintain climatological consistency with standard ETCCDI/WMO guidelines (Zhang et al., 2011; Seneviratne et al., 2021) and to ensure a statistically robust sample size. This sample size is critical for evaluating multi-level cluster stability, composite precursor dynamics, and trend significance, in particular for vertically decoupled or upper-tropospheric regimes that occur less frequently. Third, while Rome provides a highly representative reference location for urbanized coastal environments in the Central Mediterranean, where large-scale synoptic drivers interact with mesoscale sea-breeze dynamics and urban microclimates (Di Bernardino et al., 2022), the present analysis focuses on a single geographical location. Establishing this diagnostic framework at a single site was instrumental for developing and rigorously testing the multi-level clustering methodology across 35 years of tropospheric data. However, regional variations in topography, coastal proximity, and synoptic exposure across the Mediterranean basin may influence vertical thermodynamic coupling. Extending this diagnostic

framework to a broader network of Mediterranean coastal and inland locations constitutes a natural perspective for future work, enabling a regional assessment of vertical extreme regimes and their evolution under climate change.

Despite these limitations, the proposed framework, by moving beyond the traditional surface-based perspective, shows that the vertical organization of the atmospheric column provides key information on the physical nature of Mediterranean heat extremes that cannot be inferred from near-surface temperature alone. Distinguishing between vertically coupled and decoupled regimes offers a physically based framework for interpreting the processes leading to the development of EWEs and for assessing their potential implications for climate-related impacts.

5 Conclusions

This study investigated the vertical structure and the associated atmospheric dynamics of EWEs over Rome using ERA5 pressure-level data over the 1991–2025 period. By combining multi-level thermal anomaly diagnostics, multivariate analysis, synoptic composite maps, precursor thermal anomaly evolution, and air-mass backward trajectories, distinct thermodynamic and dynamical regimes governing EWEs in the Central Mediterranean were identified. In this context, the precursor analysis successfully unveiled the vertically decoupled or aligned thermodynamic pathways that precede each regime, providing a process-oriented understanding of extreme heat development prior to its surface onset. Furthermore, seasonal analysis demonstrates that the identified EWRs represent persistent, structurally coherent atmospheric modes rather than artifacts of seasonal aggregation or outlier-driven composites. The long-term analysis reveals a marked increase in the frequency of EWEs over recent decades, with a significant acceleration observed after 2015. This trend is primarily driven by a higher occurrence of vertically coupled events, specifically the *Full Column* category corresponding to the *Extreme Deep* and *Standard Deep* EWRs, characterized by significant warming extending to a large portion of the tropospheric column. Conversely, the average duration and mean thermal intensity of individual events have remained relatively stable over the 35-year period. This implies that the recent growth in regional thermal stress is primarily driven by a higher recurrence frequency of deep-column anomalies rather than by the systematic prolongation or amplification of single episodes.

Rather than reflecting an intrinsic change in atmospheric blocking behaviour, these findings point to a higher probability that persistent ridge patterns become vertically coupled across the column. This evolution has important implications for climate-risk assessment, as vertically coupled events sustain tropospheric thermal loads more efficiently and can suppress mesoscale pressure gradients, thereby reducing the cooling effectiveness of local mitigating mechanisms such as sea-breeze circulations.

Future work should evaluate the robustness of this framework across different Mediterranean sectors to assess its regional scalability, while incorporating formal non-parametric statistical testing to rigorously confirm category-specific temporal trends and potential seasonal expansions. Furthermore, utilizing higher-resolution urban climate models and convection-permitting simulations will be essential to clarify the precise, fine-scale contributions of urban canopy processes and complex coastal circulations to the vertical structure of extreme heat.

Appendix A

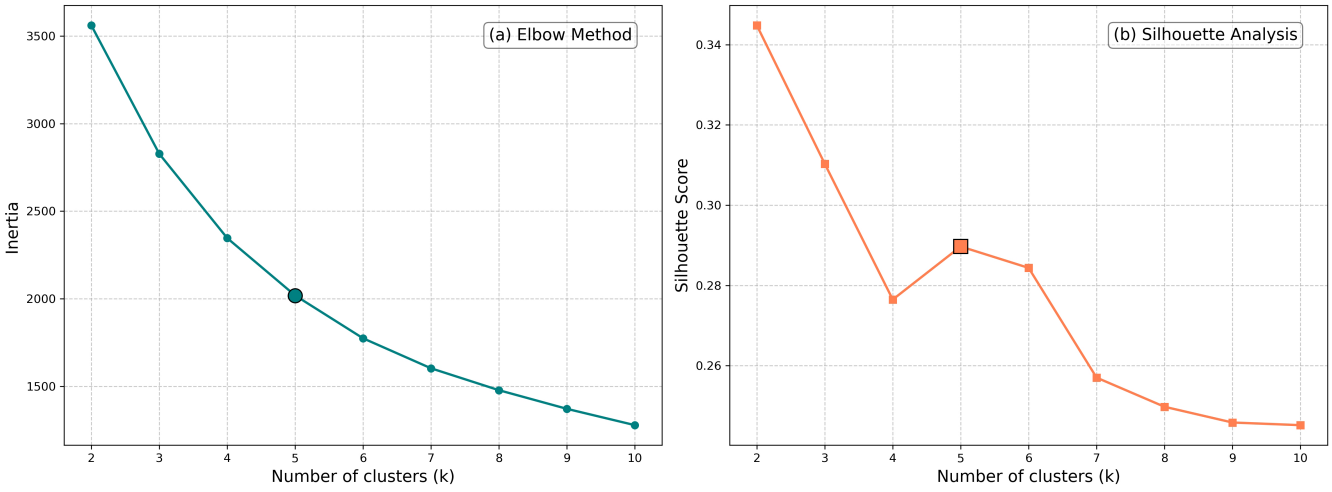

Figure A1. Results of **(a)** Elbow Method and **(b)** Silhouette Analysis used for the identification of the correct number of clusters.

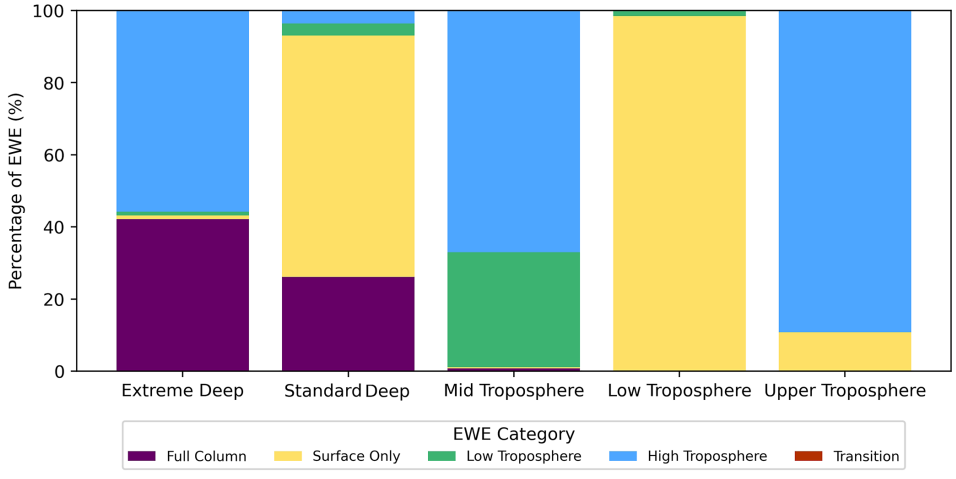

Figure A2. Relative distribution (%) of the five EWE categories within each K-means cluster (i.e., EWR) identified from the vertical temperature anomaly profiles.

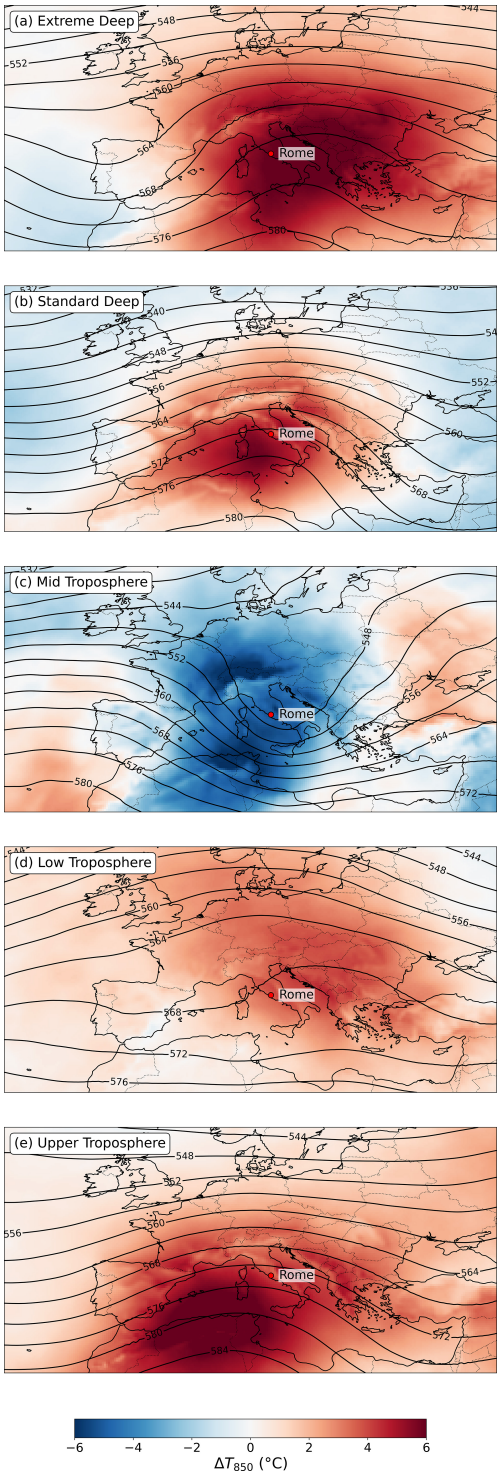

Figure A3. ERA5 synoptic composite maps for the five EWRs during the spring season (MAM): **(a)** *Extreme Deep*, **(b)** *Standard Deep*, **(c)** *Mid Troposphere*, **(d)** *Low Troposphere*, and **(e)** *Upper Troposphere*. Each map represents the average atmospheric state obtained by averaging temperature anomaly at 850 hPa, ΔT_{850}, (shaded contours, in °C) and geopotential height at 500 hPa, Z_{500} (solid, black lines, in dam).

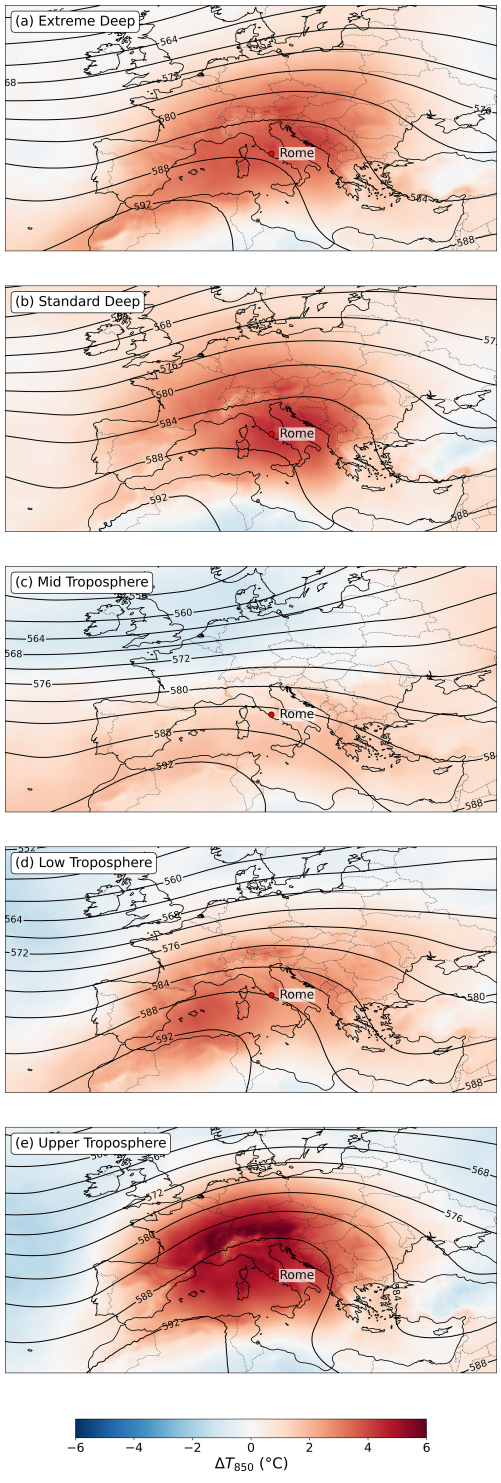

Figure A4. ERA5 synoptic composite maps for the five EWRs during the summer season (JJA): **(a)** *Extreme Deep*, **(b)** *Standard Deep*, **(c)** *Mid Troposphere*, **(d)** *Low Troposphere*, and **(e)** *Upper Troposphere*. Each map represents the average atmospheric state obtained by averaging temperature anomaly at 850 hPa, ΔT_{850}, (shaded contours, in °C) and geopotential height at 500 hPa, Z_{500} (solid, black lines, in dam).

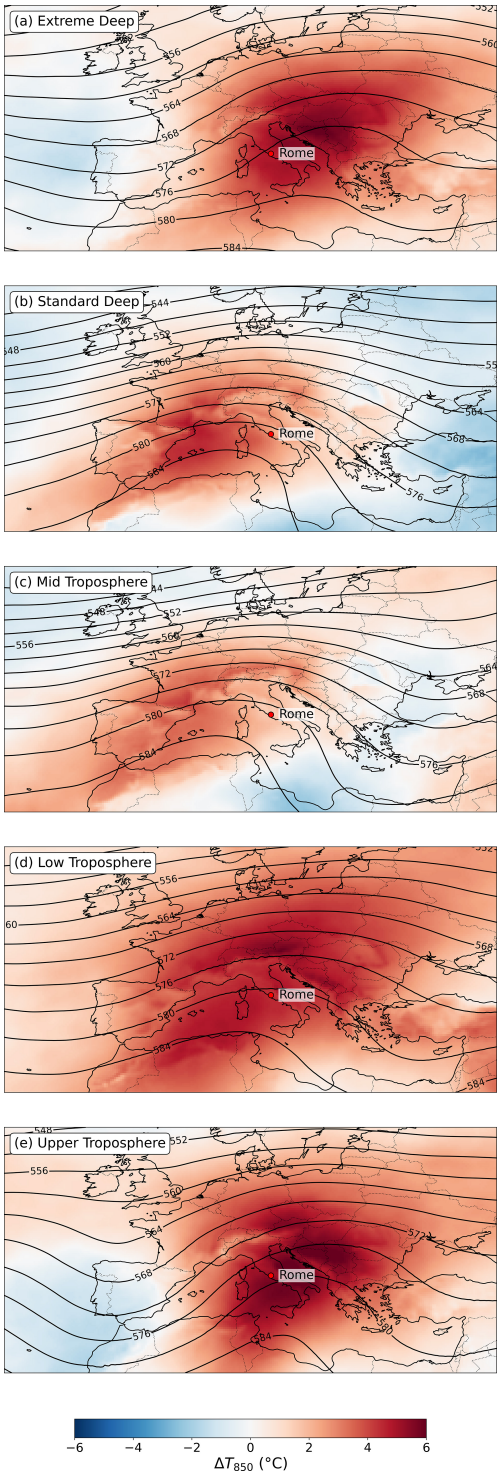

Figure A5. ERA5 synoptic composite maps for the five EWRs during the autumn season (SON): **(a)** *Extreme Deep*, **(b)** *Standard Deep*, **(c)** *Mid Troposphere*, **(d)** *Low Troposphere*, and **(e)** *Upper Troposphere*. Each map represents the average atmospheric state obtained by averaging temperature anomaly at 850 hPa, ΔT_{850}, (shaded contours, in °C) and geopotential height at 500 hPa, Z_{500} (solid, black lines, in dam).

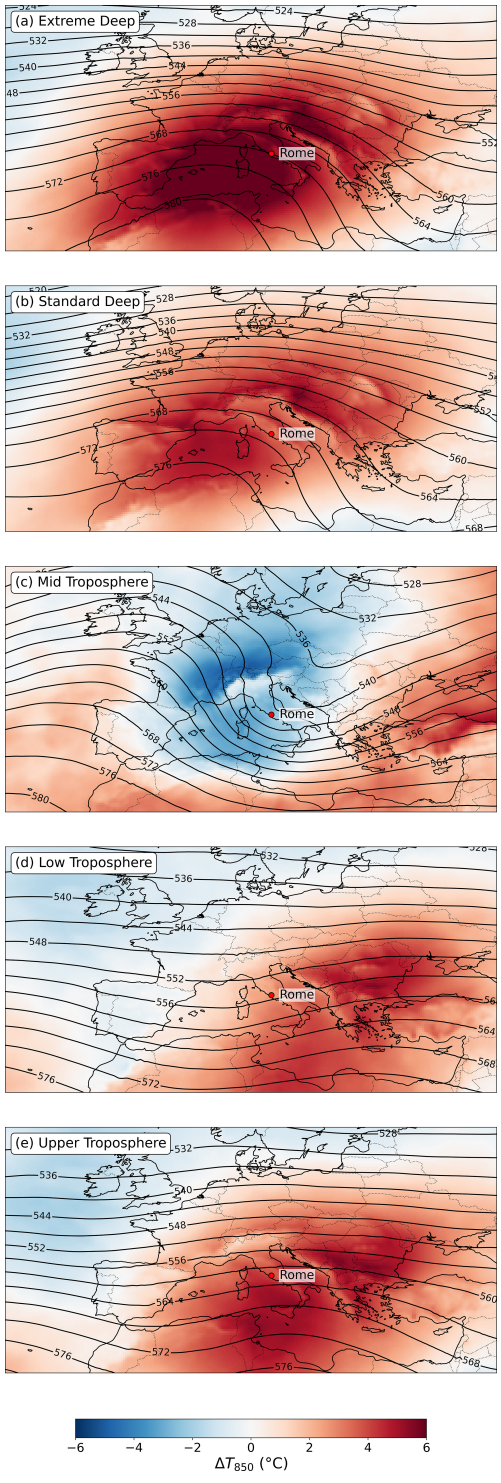

Figure A6. ERA5 synoptic composite maps for the five EWRs during the winter season (DJF): **(a)** *Extreme Deep*, **(b)** *Standard Deep*, **(c)** *Mid Troposphere*, **(d)** *Low Troposphere*, and **(e)** *Upper Troposphere*. Each map represents the average atmospheric state obtained by averaging temperature anomaly at 850 hPa, ΔT_{850}, (shaded contours, in °C) and geopotential height at 500 hPa, Z_{500} (solid, black lines, in dam).

Code and data availability. The detection and analysis scripts rely on standard Python libraries, including xarray, numpy, scipy, pandas, sklearn, matplotlib, and cartopy, and are designed to process ERA5 reanalysis data in NetCDF format. Codes are available upon request.

All data used in this study are publicly available. Reanalysis products can be found in the Copernicus Data Store repository, accessible at https://cds.climate.copernicus.eu/ (last access: 7 July 2026).

Author contributions. ADB: conception, formal analysis, methodology, resources, data curation, investigation, software, writing (original draft preparation, review & editing), funding acquisition; SC: conception, formal analysis, methodology, writing (review & editing); AMI: conception, methodology, writing (review & editing); AMS: conception, formal analysis, methodology, supervision, writing (review & editing).

Competing interests. The contact author has declared that none of the authors has any competing interests.

Disclaimer. Publisher's note: Copernicus Publications remains neutral with regard to jurisdictional claims made in the text, published maps, institutional affiliations, or any other geographical representation in this paper. The authors bear the ultimate responsibility for providing appropriate place names. Views expressed in the text are those of the authors and do not necessarily reflect the views of the publisher.

Acknowledgements. We thank the European Centre for Medium-Range Weather Forecasts (ECMWF) for providing the ERA5 reanalysis data.

Financial support. This study was partially funded by "Progetti di Ateneo Piccoli 2025" of Sapienza University of Rome, "Changes in the lower troposphere induced by extreme heat events: mechanisms and implications" (Prot. RP12519984FF5C09).

Review statement. This paper was edited by Paul O'Gorman and reviewed by Ondrej Lhotka and one anonymous referee.

References

Beck, H. E., Zimmermann, N. E., McVicar, T. R., Vergopolan, N., Berg, A., and Wood, E. F.: Present and future Köppen-Geiger climate classification maps at 1 km resolution, Sci. Data, 5, 180214, https://doi.org/10.1038/sdata.2018.214, 2018.

Bedoya-Valestt, S., Azorin-Molina, C., Plaza-Martin, N. P., Minola, L., Gimeno, L., Andres-Martin, M., Vicente-Serrano, S. M., and Chen, D.: Weaker and more frequent Mediterranean Sea breezes in a warming climate, Sci. Rep., https://doi.org/10.1038/s41598-026-47025-4, 2026.

Bolton, D.: The computation of equivalent potential temperature, Mon. Weather Rev., 108, 1046–1053, https://doi.org/10.1175/1520-0493(1980)108<1046:TCOEPT>2.0.CO;2, 1980.

C3S/ECMWF and WMO: C3S-WMO European State of the Climate 2025, https://doi.org/10.24381/zy93-sb27, 2026.

Capozzi, V., Di Bernardino, A., and Budillon, G.: Changes in large-scale circulation behind the increase in extreme heat events in the Apennines (Italy), Atmos. Res., 319, 108013, https://doi.org/10.1016/j.atmosres.2025.108013, 2025.

Cecilia, A., Casasanta, G., Petenko, I., Conidi, A., and Argentini, S.: Measuring the urban heat island of Rome through a dense weather station network and remote sensing imperviousness data, Urban Clim., 47, 101355, https://doi.org/10.1016/j.uclim.2022.101355, 2023.

Cohen, J., Zhang, X., Francis, J., Jung, T., Kwok, R., Overland, J., Ballinger, T. J., Bhatt, U. S., Chen, H. W., Coumou, D., Feldstein, S., Gu, H., Handorf, D., Henderson, G., Ionita, M., Kretschmer, M., Laliberte, F., Lee, S., Linderholm, H. W., Maslowski, W., Peings, Y., Pfeiffer, K., Rigor, I., Semmler, T., Stroeve, J., Taylor, P. C., Vavrus, S., Vihma, T., Wang, S., Wendisch, M., Wu, Y., and Yoon, J.: Divergent consensuses on Arctic amplification influence on midlatitude severe winter weather, Nat. Clim. Change, 10, 20–29, https://doi.org/10.1038/s41558-019-0662-y, 2020.

Cos, J., Doblas-Reyes, F., Jury, M., Marcos, R., Bretonnière, P.-A., and Samsó, M.: The Mediterranean climate change hotspot in the CMIP5 and CMIP6 projections, Earth Syst. Dynam., 13, 321–340, https://doi.org/10.5194/esd-13-321-2022, 2022.

Coumou, D., Di Capua, G., Vavrus, S., Wang, L., and Wang, S.: The influence of Arctic amplification on mid-latitude summer circulation, Nat. Commun., 9, 2959, https://doi.org/10.1038/s41467-018-05256-8, 2018.

Cramer, W., Guiot, J., Fader, M., Garrabou, J., Gattuso, J. P., Iglesias, A., Lange, M. A., Lionello, P., Llasat, M. C., Paz, S., Peñuelas, J., Snoussi, M., Toreti, A., Tsimplis, M. N., and Xoplaki, E.: Climate change and interconnected risks to sustainable development in the Mediterranean, Nat. Clim. Chang., 8, 972–980, https://doi.org/10.1038/s41558-018-0299-2, 2018.

Di Bernardino, A., Iannarelli, A. M., Casadio, S., Mevi, G., Campanelli, M., Casasanta, G., Cede, A., Tiefengraber, M., Spinei, E., and Cacciani, M.: On the effect of sea breeze regime on aerosols and gases properties in the urban area of Rome, Italy, Urban Clim., 37, 100842, https://doi.org/10.1016/j.uclim.2021.100842, 2021.

Di Bernardino, A., Mazzarella, V., Pecci, M., Casasanta, G., Cacciani, M., and Ferretti, R.: Interaction of the sea breeze with the urban area of Rome: WRF mesoscale and WRF large-eddy simulations compared to ground-based observations, Bound.-Lay. Meteorol., 185, 333–363, https://doi.org/10.1007/s10546-022-00734-5, 2022.

Di Bernardino, A., Falasca, S., Iannarelli, A. M., Casadio, S., and Siani, A. M.: Effect of heatwaves on urban sea breeze, heat island intensity, and outdoor thermo-hygrometric comfort in Rome (Italy), Urban Clim., 52, 101735, https://doi.org/10.1016/j.uclim.2023.101735, 2023.

Di Bernardino, A., Iannarelli, A. M., Casadio, S., and Siani, A. M.: Winter warm spells over Italy: Spatial–temporal variation and

large-scale atmospheric circulation, Int. J. Climatol., 44, 1262–1275, https://doi.org/10.1002/joc.8388, 2024.

Di Bernardino, A., Argentini, S., Brattich, E., Campanelli, M., Casasanta, G., Cecilia, A., Erriu, M., Falasca, S., Faggi, A., and Siani, A. M.: Influence of atmospheric parameters on the interaction between Urban Heat and Pollution Islands in a Mediterranean coastal city, Atmos. Res., 108702, https://doi.org/10.1016/j.atmosres.2025.108702, 2025.

Draxler, R. R. and Rolph, G. D.: HYSPLIT (HYbrid Single-Particle Lagrangian Integrated Trajectory) model access via NOAA ARL READY website, NOAA Air Resources Laboratory, Silver Spring, MD, 25, http://ready.arl.noaa.gov/HYSPLIT.php (last access: 2 September 2026), 2010.

Duchez, A., Frajka-Williams, E., Josey, S. A., Evans, D. G., Grist, J. P., Marsh, R., McCarthy, G. D., Sinha, B., Berry, D. I., and Hirschi, J. J.: Drivers of exceptionally cold North Atlantic Ocean temperatures and their link to the 2015 European heat wave, Environ. Res. Lett., 11, 074004, https://doi.org/10.1088/1748-9326/11/7/074004, 2016.

Fix-Hewitt, F., Zeileis, A., Stucke, I., Stauffer, R., and Mayr, G. J.: Properties and characteristics of atmospheric deserts over Europe: a first statistical analysis, Weather Clim. Dynam., 7, 17–35, https://doi.org/10.5194/wcd-7-17-2026, 2026a.

Fix-Hewitt, F., Zeileis, A., Stucke, I., Stauffer, R., and Mayr, G. J.: Co-occurrence of atmospheric deserts over Europe with strong positive temperature anomalies, thunderstorms, and dust events, Weather Clim. Dynam., 7, 2133–2153, https://doi.org/10.5194/wcd-7-2133-2026, 2026b.

Francis, J. A., Vavrus, S. J., and Cohen, J.: Amplified Arctic warming and mid-latitude weather: New perspectives on emerging connections, WIRES Climate Change, 8, e474, https://doi.org/10.1002/wcc.474, 2017.

Giannakopoulos, C., Le Sager, P., Bindi, M., Moriondo, M., Kostopoulou, E., and Goodess, C. M.: Climatic changes and associated impacts in the Mediterranean resulting from a 2 C global warming, Glob. Planet. Change, 68, 209–224, https://doi.org/10.1016/j.gloplacha.2009.06.001, 2009.

Giorgi, F.: Climate change hot-spots, Geophys. Res. Lett., 33, L08707, https://doi.org/10.1029/2006GL025734, 2006.

Gobbi, G. P., Barnaba, F., Di Liberto, L., Bolignano, A., Lucarelli, F., Nava, S., Perrino, C., Pietrodangelo, A., Basart, S., Costabile, F., Dionisi, D., Rizza, U., Canepari, S., Sozzi, R., Morelli, M., Manigrasso, M., Drewnick, F., Struckmeier, C., Poenitz, K., and Wille, H.: An inclusive view of Saharan dust advections to Italy and the Central Mediterranean, Atmos. Environ., 201, 242–256, https://doi.org/10.1016/j.atmosenv.2019.01.002, 2019.

Hassoun, A. E. R., Mojtahid, M., Merheb, M., Lionello, P., Gattuso, J. P., and Cramer, W.: Climate change risks on key open marine and coastal mediterranean ecosystems, Sci. Rep., 15, 24907, https://doi.org/10.1038/s41598-025-07858-x, 2025.

Hersbach, H. and National Center for Atmospheric Research (NCAR) Staff (Eds.): The Climate Data Guide: ERA5 atmospheric reanalysis, https://climatedataguide.ucar.edu/climate-data/era5-atmospheric-reanalysis, last access: 7 July 2026.

Hersbach, H., Bell, B., Berrisford, P., Hirahara, S., Horányi, A., Muñoz-Sabater, J., Nicolas, J., Peubey, C., Radu, R., Schepers, D., Simmons, A., Soci, C., Abdalla, S., Abellan, X., Balsamo, G., Bechtold, P., Biavati, G., Bidlot, J., Bonavita, M., De Chiara, G., Dahlgren, P., Dee, D., Diamantakis, M., Dragani, R., Flemming, J., Forbes, R., Fuentes, M., Geer, A., Haimberger, L., Healy, S., Hogan, R. J., Hólm, E., Janisková, M., Keeley, S., Laloyaux, P., Lopez, P., Lupu, C., Radnoti, G., de Rosnay, P., Rozum, I., Vamborg, F., Villaume, S., and Thépaut, J.-N.: The ERA5 global reanalysis, Q. J. R. Meteorol. Soc., 146, 1999–2049, https://doi.org/10.1002/qj.3803, 2020.

Hirsch, A. L. and King, M. J.: Atmospheric and land surface contributions to heatwaves: An Australian perspective, J. Geophys. Res.-Atmos., 125, e2020JD033223, https://doi.org/10.1029/2020JD033223, 2020.

Hirsch, R. M. and Slack, J. R.: A nonparametric trend test for seasonal data with serial dependence, Water Resour. Res., 20, 727–732, https://doi.org/10.1029/WR020i006p00727, 1984.

Hotz, B., Papritz, L., and Röthlisberger, M.: Understanding the vertical temperature structure of recent record-shattering heatwaves, Weather Clim. Dynam., 5, 323–343, https://doi.org/10.5194/wcd-5-323-2024, 2024.

Hotz, B., Wernli, H., Röthlisberger, M., and Noyelle, R.: Global characterisation of the vertical temperature anomaly structure of heat extremes over land in ERA5, Weather Clim. Dynam., 7, 1875–1897, https://doi.org/10.5194/wcd-7-1875-2026, 2026.

Kendall, M. G. and Gibbons, J. D.: Rank correlation methods, Griffin, London, ISBN 0852641990, 1962.

Lhotka, O. and Kyselý, J.: Three-dimensional analysis reveals diverse heat wave types in Europe, Commun. Earth Environ., 5, 323, https://doi.org/10.1038/s43247-024-01497-2, 2024.

Lhotka, O., Kyselý, J., and Plavcová, E.: Evaluation of major heat waves' mechanisms in EURO-CORDEX RCMs over Central Europe, Clim. Dynam., 50, 4249–4262, https://doi.org/10.1007/s00382-017-3873-9, 2018.

Lin, F. and Li, C.: Do economic impacts of heat waves vary across climates? Evidence from Chinese cities, Urban Clim., 67, 102853, https://doi.org/10.1016/j.uclim.2026.102853, 2026.

Mahecha, M. D., Bastos, A., Bohn, F. J., Eisenhauer, N., Feilhauer, H., Hickler, T., Kalesse-Los, H. , Migliavacca, M., Otto, F. E. L., Peng, J., Sippel, S., Tegen, I., Weigelt, A., Wendisch, M., Wirth, C., Al-Halbouni, D., Deneke, H., Doktor, D., Dunker, S., Duveiller, G., Ehrlich, A., Foth, A., García-García, A., Guerra, C. A., Guimarães-Steinicke, C., Hartmann, H., Henning, S., Herrmann, H., Hu, P., Ji, C., Kattenborn, T., Kolleck, N., Kretschmer, M., Kühn, I., Luttkus, M. L., Maahn, M., Mönks, M., Mora, K., Pöhlker, M., Reichstein, M., Rüger, N., Sánchez-Parra, B., Schäfer, M., Stratmann, F., Tesche, M., Wehner, B., Wieneke, S., Winkler, A. J., Wolf, S., Zaehle, S., Zscheischler, J., and Quaas, J.: Biodiversity and climate extremes: Known interactions and research gaps, Earths Future, 12, e2023EF003963, https://doi.org/10.1029/2023EF003963, 2024.

Mann, H. B.: Nonparametric tests against trend, Econometrica, 245–259, https://doi.org/10.2307/1907187, 1945.

Margolis, H. G.: Heat Waves and Rising Temperatures: Human Health Impacts and the Determinants of Vulnerability, in: Climate Change and Global Public Health, edited by: Pinkerton, K. E. and Rom, W. N., Respiratory Medicine, Humana, Cham, https://doi.org/10.1007/978-3-030-54746-2_7, 2020.

Miralles, D. G., Teuling, A. J., Van Heerwaarden, C. C., and Vilà-Guerau de Arellano, J.: Mega-heatwave temperatures due to combined soil desiccation and atmospheric heat accumulation,

Nat. Geosci., 7, 345–349, https://doi.org/10.1038/ngeo2141, 2014.

Molina, M. O., Sánchez, E., and Gutiérrez, C.: Future heat waves over the Mediterranean from an Euro-CORDEX regional climate model ensemble, Sci. Rep., 10, 8801, https://doi.org/10.1038/s41598-020-65663-0, 2020.

Nogueira, M., Hurduc, A., Ermida, S., Lima, D. C. A., Soares, P. M. M., Johannsen, F., and Dutra, E.: Assessment of the Paris urban heat island in ERA5 and offline SURFEX-TEB (v8.1) simulations using the METEOSAT land surface temperature product, Geosci. Model Dev., 15, 5949–5965, https://doi.org/10.5194/gmd-15-5949-2022, 2022.

Pastor, F., Valiente, J. A., and Khodayar, S.: A warming Mediterranean: 38 years of increasing sea surface temperature, Remote Sens., 12, 2687, https://doi.org/10.3390/rs12172687, 2020.

Perkins-Kirkpatrick, S. E. and Lewis, S. C.: Increasing trends in regional heatwaves, Nat. Commun., 11, 3357, https://doi.org/10.1038/s41467-020-16970-7, 2020.

Pettitt, A. N.: A non-parametric approach to the change-point problem, J. Roy. Stat. Soc. C App., 28, 126–135, https://doi.org/10.2307/2346729, 1979.

Pfahl, S., Schwierz, C., Croci-Maspoli, M., Grams, C. M., and Wernli, H.: Importance of latent heat release in ascending air streams for atmospheric blocking, Nat. Geosci., 8, 610–614, https://doi.org/10.1038/ngeo2487, 2015.

Previdi, M., Smith, K. L., and Polvani, L. M.: Arctic amplification of climate change: a review of underlying mechanisms, Environ. Res. Lett., 16, 093003, https://doi.org/10.1088/1748-9326/ac1c29, 2021.

Röthlisberger, M. and Papritz, L.: Quantifying the physical processes leading to atmospheric hot extremes at a global scale, Nat. Geosci., 16, 210–216, https://doi.org/10.1038/s41561-023-01126-1, 2023.

Rousi, E., Kornhuber, K., Beobide-Arsuaga, G., Luo, F., and Coumou, D.: Accelerated western European heatwave trends linked to more-persistent double jets over Eurasia, Nat. Commun., 13, 3851, https://doi.org/10.1038/s41467-022-31432-y, 2022.

Sadhukhan, B., Mukherjee, S., and Samanta, R. K.: A study of global temperature anomalies and their changing trends due to global warming, 14th International Conference on Computational Intelligence and Communication Networks (CICN), IEEE, 660–666, https://doi.org/10.1109/CICN56167.2022.10008329, 2022.

Seneviratne, S. I., Corti, T., Davin, E. L., Hirschi, M., Jaeger, E. B., Lehner, I., Orlowsky, B., and Teuling, A. J.: Investigating soil moisture–climate interactions in a changing climate: A review, Earth-Sci. Rev., 99, 125–161, https://doi.org/10.1016/j.earscirev.2010.02.004, 2010.

Seneviratne, S. I., Zhang, X., Adnan, M., Badi, W., Dereczynski, C., Di Luca, A., Ghosh, S., Iskandar, I., Kossin, J., Lewis, S., Otto, F., Pinto, I., Satoh, M., Vicente-Serrano, S. M., Wehner, M., and Zhou, B.: Weather and Climate Extreme Events in a Changing Climate, in: Climate Change 2021: The Physical Science Basis, Contribution of Working Group I to the Sixth Assessment Report of the Intergovernmental Panel on Climate Change, Cambridge University Press, Cambridge, United Kingdom and New York, NY, USA, 1513–1766, https://doi.org/10.1017/9781009157896.013, 2021.

Sousa, P. M., Trigo, R. M., Barriopedro, D., Soares, P. M., and Santos, J. A.: European temperature responses to blocking and ridge regional patterns, Clim. Dyn., 50, 457–477, https://doi.org/10.1007/s00382-017-3620-2, 2018.

Stéfanon, M., Drobinski, P., D'Andrea, F., Lebeaupin-Brossier, C., and Bastin, S.: Soil moisture-temperature feedbacks at meso-scale during summer heat waves over Western Europe, Clim. Dyn., 42, 1309–1324, https://doi.org/10.1007/s00382-013-1794-9, 2014.

Woollings, T., Barriopedro, D., Methven, J., Son, S. W., Martius, O., Harvey, B., Sillmann, J., Rupo, A. R., and Seneviratne, S.: Blocking and its response to climate change, Curr. Clim. Change Rep., 4, 287–300, https://doi.org/10.1007/s40641-018-0108-z, 2018.

World Meteorological Organization: WMO Guidelines on the Calculation of Climate Normals, World Meteorological Organization, Geneva, WMO-No. 1203, ISBN 978-92-63-11203-3, 2017.

World Meteorological Organization: Commission for weather, climate, water and related environmental services and applications, Modernization of the WMO state of the climate monitoring, https://meetings.wmo.int/SERCOM-2/_layouts/15/WopiFrame.aspx?sourcedoc=%7b422E11CE-62D1-42B5-800D-D1E482C1606F%7d&file=SERCOM-2-d05-5(2)-MODERNIZATION-STATE-OF-CLIMATE-MONITORING-draft1_en.docx&action=default (last access: 7 July 2026), 2022.

World Meteorological Organization (WMO) and World Health Organization (WHO): Heatwaves and Health: Guidance on Warning-System Development, edited by: McGregor, G. R., Bessemoulin, P., Ebi, K. L., and Menne, B., World Meteorological Organization, Geneva, WMO-No. 1142, ISBN 978-92-63-11142-5, 2015.

Yue, S. and Wang, C.: The Mann-Kendall test modified by effective sample size to detect trend in serially correlated hydrological series, Water Resour. Manag., 18, 201–218, https://doi.org/10.1023/B:WARM.0000043140.61082.60, 2004.

Zhang, X., Alexander, L., Hegerl, G. C., Jones, P., Tank, A. K., Peterson, T. C., Trewin, B., and Zwiers, F. W.: Indices for monitoring changes in extremes based on daily temperature and precipitation data, WIRES Climate Change, 2, 851–870, https://doi.org/10.1002/wcc.147, 2011.

Zhu, J., Zhu, S., Yu, F., Zhang, G., and Xu, Y.: A downscaling method for ERA5 reanalysis land surface temperature over urban and mountain areas, Nat. Remote Sens. Bull., 25, 1778–1791, https://doi.org/10.11834/jrs.20211257, 2021.

Zittis, G., Hadjinicolaou, P., Almazroui, M., Bucchignani, E., Driouech, F., El Rhaz, K., Kurnaz, L., Nikulin, G., Ntoumos, A., Ozturk, T., Proestos, Y., Stenchikov, G., Zaaboul, R., and Lelieveld, J.: Business-as-usual will lead to super and ultra-extreme heatwaves in the Middle East and North Africa, Npj Clim. Atmos. Sci., 4, 20, https://doi.org/10.1038/s41612-021-00178-7, 2021.

Zschenderlein, P., Fink, A. H., Pfahl, S., and Wernli, H.: Processes determining heat waves across different European climates, Q. J. R. Meteorol. Soc., 145, 2973–2989, https://doi.org/10.1002/qj.3599, 2019.